

The GECKOS Survey: Extraplanar ionised gas in star-forming galaxies from eDIG to galaxy-scale winds

R. Elliott^{1,2}, D.B. Fisher^{1,2}, B. Mazzilli Ciraulo^{1,2}, A. Fraser-McKelvie^{3,2}, M. R. Hayden⁴, M. Martig⁵, J. van de Sande^{6,2}, A. J. Battisti^{7,8,2}, J. Bland-Hawthorn^{9,2}, A. D. Bolatto¹⁰, T. H. Brown¹¹, B. Catinella^{7,2}, F. Combes^{12,13}, L. Cortese^{7,2}, T. A. Davis¹⁴, E. Emsellem^{3,15}, D. A. Gadotti¹⁶, F. Pinna^{20,21}, T. H. Puzia²², L. A. Silva-Lima²³, L. M. Valenzuela²⁴, G. van de Ven²⁵,

¹Centre for Astrophysics and Supercomputing, Swinburne University of Technology, Hawthorn, VIC 3122, Australia

²ARC Centre of Excellence for All Sky Astrophysics in 3 Dimensions (ASTRO 3D), Australia

³European Southern Observatory, Karl-Schwarzschild-Straße 2, Garching, 85748, Germany

⁴Homer L. Dodge Department of Physics & Astronomy, University of Oklahoma, 440 W. Brooks St., Norman, OK 73019, USA

⁵Astrophysics Research Institute, Liverpool John Moores University, 146 Brownlow Hill, Liverpool L3 5RF, UK

⁶School of Physics, University of New South Wales, Sydney, NSW 2052, Australia

⁷International Centre for Radio Astronomy Research (ICRAR), The University of Western Australia, M468, 35 Stirling Highway, Crawley, WA 6009, Australia

⁸Research School of Astronomy and Astrophysics, Australian National University, Cotter Road, Weston Creek, ACT 2611, Australia

⁹Sydney Institute for Astronomy, School of Physics, A28, The University of Sydney, NSW, 2006, Australia

¹⁰Department of Astronomy, University of Maryland, College Park, MD 20742, USA

¹¹National Research Council of Canada, Herzberg Astronomy and Astrophysics Research Centre, 5071 W. Saanich Rd. Victoria, BC, V9E 2E7, Canada

¹²Observatoire de Paris, LUX, CNRS, PSL University, Sorbonne University, 75014 Paris, France

¹³Collège de France, 11 Pl. Marcelin Berthelot, 75231 Paris, France

¹⁴Cardiff Hub for Astrophysics Research & Technology, School of Physics & Astronomy, Cardiff University, Queens Buildings, Cardiff, CF24 3AA, UK

¹⁵Univ Lyon, Univ Lyon1, ENS de Lyon, CNRS, Centre de Recherche Astrophysique de Lyon UMR5574, F-69230 Saint-Genis-Laval France

¹⁶Centre for Extragalactic Astronomy, Department of Physics, Durham University, South Road, Durham DH1 3LE, UK

¹⁷Cosmic Dawn Center (DAWN), Denmark

¹⁸NSF's NOIRLab, 950 N. Cherry Avenue, Tucson, AZ 85719, USA

¹⁹Instituto de Astrofísica de Canarias, calle Vía Láctea s/n, E-38205 La Laguna, Tenerife, Spain

²⁰Departamento de Astrofísica, Universidad de La Laguna, Avenida Astrofísico Francisco Sánchez s/n, E-38206 La Laguna, Spain

²¹Instituto de Astrofísica, Pontificia Universidad Católica de Chile, Avenida Vicuña Mackenna 4860, 7820436, Macul, Santiago, Chile

²²Núcleo de Astrofísica, Universidade Cidade de São Paulo, Rua Galvão Bueno, 868, São Paulo, Brazil

²³Universitäts-Sternwarte, Fakultät für Physik, Ludwig-Maximilians-Universität München, Scheinerstr. 1, 81679 München, Germany

²⁴Department of Astrophysics, University of Vienna, Türkenschanzstraße 17, 1180 Vienna, Austria

Accepted XXX. Received YYY; in original form ZZZ

ABSTRACT

We map the extraplanar gas, with \sim 50–200 pc resolution, in nine star-forming galaxies using Multi-Unit Spectroscopic Explorer (MUSE) observations from the GECKOS VLT Large Program targeting edge-on galaxies with similar stellar mass as the Milky Way. The narrow range in stellar mass (± 0.35 dex) of the GECKOS sample makes it ideal for studying trends with star formation rate (SFR). We find strong extraplanar emission reaching \sim 2–8 kpc from the disk midplane in all targets with $\text{SFR} \geq 1 \text{ M}_\odot \text{ yr}^{-1}$. Targets with $\text{SFR} \geq 5 \text{ M}_\odot \text{ yr}^{-1}$ have brighter, more extended H α emission compared to lower SFR targets. In high-SFR systems, the gas velocity dispersion ($\sigma_{\text{H}\alpha}$) shows a biconical morphology, consistent with the expectation of outflows. This agrees with previous works suggesting high velocity dispersion in a biconical shape is a good means to identify outflows. We find mixed results using line diagnostics ($[\text{OIII}]_{5007}/\text{H}\beta$ - $[\text{NII}]/\text{H}\alpha$ and $\sigma_{\text{H}\alpha}$ - $[\text{SII}]/\text{H}\alpha$) to spatially resolve ionisation mechanisms across the extraplanar gas. The highest $[\text{NII}]/\text{H}\alpha$ are the extraplanar gas of the highest SFR systems, yet main-sequence galaxies have the highest $[\text{OIII}]/\text{H}\beta$. While the morphology of $[\text{NII}]/\text{H}\alpha$ may be useful to identify outflows, the absolute value of the line ratio alone may not distinguish strong outflows from extraplanar gas of main-sequence galaxies. The ubiquitous extraplanar emission can be interpreted as the result of feedback, in the form of large-scale winds for starbursts or smaller-scale galactic fountains for main-sequence galaxies. Moreover, shock-heating may ionise gas at the interface of the disk and the circumgalactic medium, independent of the source of the gas.

1 INTRODUCTION

Extraplanar diffuse interstellar gas (eDIG) is commonly seen around star-forming galaxies (e.g. Dettmar 1990; Rand 1996; Rossa & Dettmar 2003). Many mechanisms are invoked to explain its origin,

including stellar feedback-driven galactic fountains (Shapiro & Field 1976), relic gas from galactic outflows (López-Cobá et al. 2019), leaky HII regions (Haffner et al. 2009) and post-asymptotic giant branch stars in the thick stellar disk (Flores-Fajardo et al. 2011). Recent work on the EDGE-CALIFA survey (Levy et al. 2019) ar-

gues that the vertical gas kinematics tend to favor an internal driving mechanism from the disk, i.e. stellar feedback, as the main source of eDIG. [González-Díaz et al. \(2024\)](#) also find connections between the distribution of young massive star feedback and minor axis-parallel ionization profiles in a sample with modest SFR.

Neither the observational differences between eDIG and galactic winds nor the strength of these differences is well established in main-sequence galaxies. The high velocity and turbulent internal motions of winds create a plausible environment for shocks, which may be diagnosed using optical emission line ratios ([Dopita & Sutherland 1996](#)). Shock-excited gas typically exhibits elevated velocity dispersion and characteristic elevated optical emission line ratios. These signatures are used by studies to separate shock-ionized gas from star-formation-ionized gas. ([Rich et al. 2010, 2011, 2015; Ho et al. 2014, 2016; Kewley et al. 2019a](#)).

Galactic winds (i.e. outflows) are a specific type of extraplanar gas that play a key role in galaxy evolution. They are large-scale galaxy mass ejecta that have suppressive effects on star formation in the host galaxy. These ejecta are driven by supernovae explosions (SNe), radiation from young stars, and Active Galactic Nuclei (AGN). Outflows can carry interstellar medium (ISM) material far beyond the disk of the host galaxy (reviews [Veilleux et al. 2020a; Thompson & Heckman 2024](#)). Cosmological simulations find that mass-loss via outflows are a required component of the simulations, to match observations stellar masses and star formation rates (SFR) ([Somerville & Davé 2015; Naab & Ostriker 2017; Thompson & Heckman 2024](#)). There is, however, currently no theoretical consensus to describe the energetics of outflows (for example, see review by [Thompson & Heckman 2024](#)). Moreover, resolved surveys of galaxies with outflows are rare (see discussion in [Veilleux et al. 2020b](#)). Recent work with optical IFU instruments is changing this (e.g. [Reichardt Chu et al. 2025](#)).

The last 15 years have seen a significant number of resolved observations of optical emission lines in extraplanar gas of both outflows and super-main-sequence systems ([Sharp & Bland-Hawthorn 2010; Bik et al. 2018; López-Cobá et al. 2020; Reichardt Chu et al. 2022, 2024; McPherson et al. 2023; Watts et al. 2024](#)). Whilst these observations provide the opportunity to detect and study wind-shocks using line ratios, there is no clear consensus on the presence of shocks in the existing observations. [Ho et al. \(2014\)](#) argue that, based on observed line ratios, shock-ionized gas is very common in their sample of star-forming galaxies. Conversely, [Bik et al. \(2018\)](#) found, using MUSE imaging, that the gas above the center of the outflowing galaxy ESO338-IG04 has emission line ratios more consistent with photoionisation than shock-ionization. [Chisholm et al. \(2017\)](#) make a similar finding from using absorption lines to study a sample of outflowing galaxies. We note that moderately elevated emission line ratios in extraplanar gas do not *a priori* require shocks to exist: weak dust-shielding above galactic planes allow for harder radiation fields, resulting in elevated extraplanar line ratios ([Kewley et al. 2019a](#)).

This article uses GECKOS survey (Generalising Edge-on galaxies and their Chemical bimodalities, Kinematics, and Outflows out to Solar environments, [van de Sande et al. 2023](#)) IFS data of nine edge-on galaxies (Table 1 + Fig. 1). The galaxies have masses within ± 0.3 dex of the Milky Way mass, $\sim 5 \times 10^{10} M_{\odot}$ ([Bland-Hawthorn & Gerhard 2016](#)), and SFRs varying over an order of magnitude (SFR $\sim 0.2\text{--}2 M_{\odot} \text{ yr}^{-1}$). We exploit deep MUSE observations from GECKOS to make resolved ($\sim 50\text{--}200$ pc) studies of the kinematics and line-ratios of extraplanar gas across diverse star forming environments.

Sections 2.1-2.2 outline details of the GECKOS survey observations. Section 2.3 describes the GECKOS data reduction process,

and Section 2.4 describes the post-processing we performed on our reduced data. Sections 3.1-3.3 present maps made from the reduced GECKOS data, highlighting kinematic and morphological differences between galaxies in our sample. Section 3.4 outlines how these maps can be systematically broken into different regions for analysis. Section 3.5 compares surface brightness profiles from these regions in each galaxy, and 4 offers an emission line ratio analysis of our galaxy sample. 5 offers a detailed discussion of the paper's results. Note that we have assumed a standard Λ CDM cosmology for this study (i.e. $H_0 = 68 \text{ km s}^{-1} \text{ Mpc}^{-1}, \Omega_m = 0.3$).

2 METHODS

2.1 GECKOS targets in this work

The galaxies studied in this paper are part of the GECKOS survey ([van de Sande et al. 2023](#)). The GECKOS survey is a 317 hr Large Program (PI: J. van de Sande) using the Multi-Unit Spectroscopic Explorer (hereafter MUSE) instrument on Unit Telescope 4 of the Very Large Telescope (VLT). The full GECKOS sample is 36 galaxies that are selected to have stellar mass within ± 0.3 dex of the Milky Way mass ($\sim 5 \times 10^{10} M_{\odot}$), are close to edge-on, at a distance of 10-70 Mpc. GECKOS targets are chosen to span a wide range in SFR, (~ 2 dex), making the sample ideal to search for mass-controlled correlations with SFR. The MUSE observations began in 2022 and concluded in 2025. This work studies the first nine star-forming galaxies, reduced and analysed as part of the GECKOS internal data release 1, as listed in Table 1.

The galaxy sample in this paper includes three galaxies that have previously been found to host galactic winds: NGC 4666 ([Dahlem et al. 1997](#)), NGC 5775 ([Heald et al. 2006](#)), and ESO 484-036 ([Veilleux et al. 2005](#)). [Heald et al. \(2006\)](#) trace an outflow in NGC 5775 via a rotational lag between the disk and extraplanar regions. This lag is interpreted as a signature of outflowing material conserving momentum as it gradually expands into the halo. [Heald et al. \(2022\)](#) also reveal a mass outflow rate that is $\approx 40\text{--}80\%$ of the SFR by modeling the galaxy's extended radio halo. [Dahlem et al. \(1997\)](#) trace the NGC 4666 outflow by observing alignment between optical filaments, radio filaments, X-ray emission, and magnetic fields above the galaxy midplane. [Mazzilli Ciraulo et al. \(2025\)](#) carry out a detailed analysis of HI, CO and ionised gas for the NGC 4666 outflow using the same MUSE data used in this paper. They identify minor axis-parallel velocity profiles that are consistent with outflows. [Dahlem et al. \(1997\)](#) identify an outflow in ESO 484-036 via a characteristic X-shaped [NII]/H α emission line ratio enhancement emerging from the extraplanar emission in narrow-band imaging.

NGC 4666 and NGC 5775 are much closer than our other targets (around 15-20 Mpc compared to 25-70 Mpc). Therefore, MUSE tiles cover a smaller fraction of their extended emission, albeit with higher spatial resolution. We consider this difference when analysing the morphology of the extended emission.

2.2 Observations

Between 21/12/2022 and 21/8/2023, multiple observations were made for the nine galaxies in Table 1. The exposure times were set to achieve a continuum signal-to-noise (S/N) above 40 at $\mu_g = 23.5 \text{ mag arcsec}^{-2}$, which is representative of the Solar environment of the Milky Way ([Melchior & Combes 2007](#)).

Most galaxies were observed using 1-3 pointings with a 1 \times 1 arcmin 2 field-of-view, each covering different regions of the galaxy.

We implemented tiling on nearby targets to reach a major-axis position with $\mu_b = 23.5$ mag arcsec $^{-2}$. Each observation contained four ~ 9 -10 min object (O) observations and two ~ 2 -3 min offset sky observations (S), executed in an OSOOSO sequence. For targets with an SFR exceeding twice the main-sequence value at fixed stellar mass, we required MUSE tiles to cover a distance of at least 10 kpc from the galaxy midplane to identify extended winds.

2.3 Data Reduction

The data reduction process for GECKOS survey observations is described in [Fraser-Mckelvie et al. \(2025\)](#). A full description of the GECKOS data reduction workflow will be presented in [van de Sande et al. \(in prep.\)](#). We use the python package PYMUSEPIPE¹ ([Emsellem et al. 2022](#)) for data reduction, which is a wrapper for the MUSE Data Reduction Pipeline (DRP, [Weilbacher et al. 2020](#)). PYMUSEPIPE coordinated the multi-step data reduction process for observing block (OB), where each step is completed using the ESOREX package² ([ESO CPL Development Team 2015](#)).

The steps completed by ESOREX carries out bias and flat field corrections, and calibrates both wavelength and the line-spread function (LSF) for each raw pointing exposure. ESOREX then creates a geometry table to map the relative positions of each raw exposure pixel in the observed field of view. This mapping is followed by illumination corrections for each exposure, based on the twilight flat exposures associated with the current OB, as well as the flatfield corrections made earlier. ESOREX performs sky subtraction using offset sky exposures for the corresponding OB. The sky exposures are used to make a sky model, which is then fitted to each science frame. Three pointings of NGC 4666 are archival data without sky frames. The sky subtraction procedure for NGC 4666 involves using spaxels in object frames without strong emission lines. The above steps executed by ESOREX result in a datacube for each exposure. This data reduction process is described in more detail by [Mazzilli Ciraulo et al. \(2025\)](#).

We use PYMUSEPIPE and SPACEPYLOT to align the world coordinate system (WCS) of each exposure. Following an automated alignment routine, we corrected remaining spatial offsets between galaxy exposures by aligning a corresponding r band image from either the DESI Legacy image survey ([Dey et al. 2019](#)) or the Pan-STARRS survey ([Chambers et al. 2016](#)). After alignment, We stack each exposure datacube using MPDAF ([Bacon et al. 2016](#)) to make a complete datacube for each each OB. We then mosaic these complete OB cubes together to make a complete datacube for one galaxy.

2.4 Emission Line Measurement

Emission line measurement and continuum subtraction follows the same procedure as used in [Mazzilli Ciraulo et al. \(2025\)](#). Continuum subtraction was performed for each galaxy datacube using the nGIST pipeline ([Fraser-Mckelvie et al. 2025](#)), which is an extension of the original GIST pipeline ([Bittner et al. 2019](#)). nGIST builds on a number of works, which build processes compiled into the software ([Cappellari & Copin 2003; Cappellari & Emsellem 2004; Kuntschner et al. 2006; Vazdekis et al. 2010; Cappellari 2017, 2023](#)). nGIST is a modular pipeline for the analysis of integral field spectroscopic galaxy data. In this work, we employ the Continuum module, which creates continuum-only and line-only cubes after fitting the spectrum with a set of SSPs and masking emission lines. We use the

[Walcher et al. \(2009\)](#) model for continuum fitting and subtraction, as this produces the smallest residuals in H β absorption compared to other models we tested ([Vazdekis & Arimoto 1999; Bruzual & Charlot 2003](#)). Following testing in previous work on resolved outflows ([Reichardt Chu et al. 2022; McPherson et al. 2023](#)), we Voronoi bin to continuum $S/N = 7$, and fitted the rest-frame wavelength range 4750-7100Å. The Milky Way extinction is removed using the [Cardelli et al. \(1989\)](#) extinction law. The continuum model fitted to each Voronoi bin is then subtracted from the corresponding spaxels at the native MUSE resolution of 0.2". In all targets there is only sufficient continuum S/N to use this method near to the galaxy $z \lesssim \pm 1.5$ -2 kpc. Beyond this minor axis height there is no discernible shape to the continuum. In the Gaussian fitting of the emission lines, described below, we include a constant flux offset for all fits. This handles imperfections in continuum removal, and those spaxels in which the S/N is too low to estimate continuum using pPXF.

Continuum removal at wavelengths near and above ~ 6700 Å is complicated by several sky features. These features become increasingly common for larger wavelength. This then means that sky subtraction generates increasingly large residuals and imperfections redward of ~ 6700 Å. These sky features alter the continuum from the stellar population modeling. Visual inspection of the pPXF model compared to the observed continuum shows poor representation of the pPXF fit to continuum. This is likely more noticeable in the GECKOS program, as we target low surface brightness emission lines at larger scale-height, where sky lines may have greater impact. We, therefore, follow a different continuum removal approach for different emission lines. For H β and H α we must use the pPXF models to remove absorption. Moreover, the sky subtraction is well behaved in the these wavelengths and does not have an impact that we measure on the continuum model. Using the same pPXF model to remove continuum below [SII] $\lambda\lambda 6716,31$ introduces a significant systematic uncertainty. We therefore apply a local correction for continuum under the [SII] $\lambda\lambda 6716,31$ emission lines.

As described in [Mazzilli Ciraulo et al. \(2025\)](#), we identify a bandpass of ~ 50 Å around the [SII] $\lambda\lambda 6716,31$ emission lines in which to estimate a local continuum correction. The bandpass of ~ 50 Å is chosen to be small enough such that the emission line is well approximated by a simple function (linear or constant). We find that in all targets the slope of the spectrum across this area is small compared to the noise in the spectrum, and is thus consistent with negligible gradient. We remove the continuum locally by a simple linear fit to the continuum. This results in a flat continuum, with no measurable gradient, around the [SII] $\lambda\lambda 6716,31$ emission lines. We tested using a constant value instead of a straight line, and in our tests these return similar fluxes as the linear continuum removal. We test the impact of this method by measuring the change in continuum over level in a 200 Å region surrounding [SII] in spaxels both in the galaxy and in the outflow. We then compare this to the noise from the same region. We find that in the disk the continuum varies by $\sim 20\%$ of the scatter in the continuum, and in the outflow regions this reduces to $\sim 10\%$. This small difference reflects the fact that the continuum near to [SII] $\lambda\lambda 6716,31$ emission lines does not vary significantly across the small wavelength range surrounding these emission lines. Removing the continuum with this method, therefore, does not introduce measurable sources of uncertainty, and generates fewer systematic uncertainties than using pPXF for the [SII] continuum. Target ESO 484-036, the most distant in this sample, contains a strong sky-line that heavily contaminates the [SII] doublet, preventing [SII] analysis for this target.

We also reiterate that for all emission lines at larger distance from the galaxy, $z \gtrsim \pm 1.5$ -2 kpc, there is insufficient continuum S/N to

¹ <https://github.com/emsellem/pymusepipe>

² <https://www.eso.org/sci/software/cpl/esorex.html>

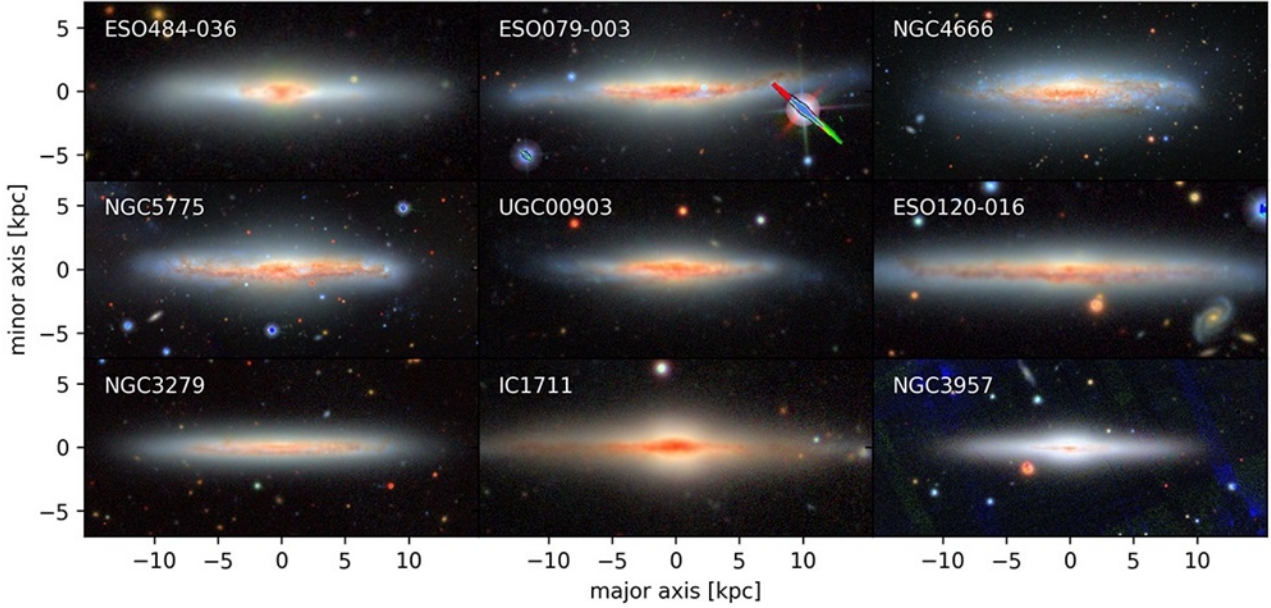


Figure 1. A collection of DESI Legacy Imaging Surveys (DR9) and Pan-STARRS-1 (DR2) colour images of the GECKOS galaxies covered in this paper. The images were produced using the g , r , and z bands with the `ASTROPY` package `MAKE_LUPTON_RGB` (Lupton et al. 2004) and an asinh stretch. The galaxies were rotated to have the photometric major axis and the dust lane (and photometric major axis) oriented horizontally, and such that the dust lane (if offset) is to the lower side of the image.

Galaxy	Distance [Mpc]	$\log(M_\star)$ [M_\odot]	SFR [$M_\odot \text{ yr}^{-1}$]	Σ_{SFR} [$10^{-2} M_\odot \text{ yr}^{-1} \text{ kpc}^{-2}$]	Spaxel Size [pc]	R_e [kpc]
ESO 484-036	69	10.5	8	10	200	5.1
ESO 079-003	36	10.6	5	4	105	6.5
NGC 4666	16	10.7	5	8	45	4.2
NGC 5775	19	10.6	5	4	55	5.8
UGC 00903	38	10.5	4	6	110	4.5
ESO 120-016	50	10.6	3	1	146	8.7
NGC 3279	30	10.3	1	1	87	5.5
IC 1711	45	10.7	1	2	131	3.8
NGC 3957	25	10.5	0.3	0.6	72	3.8

Table 1. Physical properties and MUSE observation parameters of the GECKOS galaxies analysed in this paper. Galaxies are ordered by decreasing SFR. Columns are as follows: galaxy names; distance Theureau (2023) for ESO 079-003, and Tully et al. (2023) for all others; $\log(M_\star)$ is stellar mass from van de Sande *in prep*; SFR, derived from WISE Band-4 (Cluver et al. 2017); Σ_{SFR} is SFR surface density, where $\Sigma_{SFR} = SFR/(\pi R_e^2)$; spaxel size is the resolution of the MUSE data for 0.6 arcsec resolution data; and where R_e is the effective radius (in arcsec) derived using Multi-Gaussian Expansion (MGE) models from Rutherford et al. (2025) in DECaLS r-band imaging (Blum et al. 2016).

use any formalized fitting technique. This difference is, therefore, moot for most of the extraplanar emission. The Gaussian fits include a constant offset in the fit, which is sufficient to correct continuum in these more distant regions.

After the continuum removal, each galaxy datacube is rotated such that the galaxy major axis is horizontal in the data cube. In addition, cubes are spatially rebinned by combining pixels in 3×3 squares. This rebinning yields a 0.6 arcsec resolution, which is a typical seeing value at the the VLT.

We performed single Gaussian fits to emission lines in the 3×3

rebinned datacubes using the Python package `THREADCOUNT`³, described in previous work (McPherson et al. 2023; Hamel-Bravo et al. 2024; Reichardt Chu et al. 2025; Mazzilli Ciraulo et al. 2025). We take several steps to optimise for speed. The software uses a bespoke version of the `nelder` minimisation algorithm, and a bespoke

⁴version of the Python package `lmfit`.

We run 10 iterations in which the spectrum is varied and refit. We make these variations according to a normal distribution, whose

³ <https://threadcount.readthedocs.io>

⁴ This version of `THREADCOUNT` remains in development, but is available on request from D.B. Fisher: dfisher@swin.edu.au

standard deviation is set by the observed variance. We, however, only employ MC iterations on low S/N regions of the galaxy. For spaxels with $S/N > 30$, we find that there is no advantage to MC iterations. At high S/N, fits with MC iterations return very similar parameters and uncertainty estimates as fits that do not employ the MC iteration (as single minimization run). For those spaxels with $S/N < 30$, the fit parameters and uncertainty are then taken as the mean and standard deviation of those fits.

We fitted the $\text{H}\alpha$, $\text{H}\beta$, $[\text{OIII}]\lambda 5007$, $[\text{NII}]\lambda 6548$, $[\text{NII}]\lambda 6583$, $[\text{SII}]\lambda 6716$, and $[\text{SII}]\lambda 6731$ lines for each data cube. For the results presented in this paper, we only considered emission lines in which the flux is $3\times$ greater than the fit uncertainty. We applied the same fitting procedure to versions of the data cubes that were binned to a spatial resolution of 500 pc. Both the 3×3 bin and the 500 pc bin resolution cubes will be used in this paper.

We apply extinction corrections to each fitted spaxel, by creating A_V maps from spaxel-by-spaxel Balmer decrement measurements and [Cardelli et al. \(1989\)](#) extinction curve. We only used spaxels with fitted $\text{H}\alpha$ and $\text{H}\beta$ fluxes greater than $5\times$ the flux uncertainty to create A_V maps. Spaxels with insufficient S/N for an extinction estimate were interpolated from nearby values. The interpolation may reduce the true variation of line fluxes in the data. These A_V maps were then used to correct emission line fluxes in each spaxel.

Velocity dispersions in all figures are shown with the instrumental dispersion subtracted in quadrature from the fitted dispersion to each spaxel, where $\sigma_{inst} \sim 49 \text{ km s}^{-1}$.

3 EMISSION LINE MAPS

Fig. 2 shows the 4 color maps of targets in this work. The white, diffuse light represents the $\sim 800 \text{ nm}$ continuum emission generated from MUSE cube. Emission lines are $\text{OIII} 5007$ (blue), $\text{H}\alpha$ (red) and $[\text{NII}] 6583$ (yellow). For display purposes only, we use a very low S/N cut of 2σ in Fig. 2, to err on showing all emission. For all targets, filaments of gas extend upward away from the mid-plane of the $\sim 800 \text{ nm}$ continuum image, typically this goes beyond 3 kpc from the galaxy. Similar to previous works, this figure makes it clear that extraplanar ionised gas emission is a common property of all star forming galaxies in our sample (e.g. [Rossa & Dettmar 2003](#); [Levy et al. 2019](#)). The panels of the figure are arranged by SFR, highest at the top-left and lowest at the bottom-right. This makes a clear correlation of the extension of the extraplanar gas with galaxy SFR easy to see.

The morphology of NGC 4666 is particularly interesting (for a more in depth description see [Mazzilli Ciraulo et al. 2025](#)). It is the nearest galaxy in the sample, which allows for the detailed filaments to be resolved. Individual streams of gas with width similar to the resolution limit ($\sim 45 \text{ pc}$) are visible, they extend roughly 6 kpc from the galaxy. This may be similar to the plume morphologies seen in PAH emission from JWST observations ([Fisher et al. 2025](#)). Similar plume-like structures are visible in ESO 079-003 and even ESO 120-016, the latter of which has a relatively low SFR ($\sim 3 \text{ M}_\odot \text{ yr}^{-1}$).

We note that NGC 5775 is a similar distance to NGC 4666 and has a more smooth distribution of extraplanar emission. This galaxy has a well-studied outflow (e.g. [Heald et al. 2006](#)). It has been shown to have radio continuum consistent with emission from a significant population of cosmic rays ([Heald et al. 2022](#)), which could act to smooth outflow substructure. [Stein et al. \(2019\)](#) argues for the presence of cosmic rays in the halo of NGC 4666, but the relative impact of cosmic rays between NGC 4666 compared to NGC 5775 is uncertain. It remains unclear what sets the differences in substructure of

outflows. Recent work on cloud-scale structures made with JWST, has been shown to directly test outflow theories ([Fisher et al. 2025](#)). More work, with higher spatial resolution than this data, would be informative.

Fig. 3 displays 0.6 arcsec resolution maps of $\text{H}\alpha$ flux, $\text{H}\alpha$ velocity dispersion, $[\text{NII}]/\text{H}\alpha$, and $\text{H}\alpha$ line-of-sight velocity for each galaxy in our sample. Fig. 4 displays alternative velocity dispersion maps ($\sigma_{\text{H}\alpha}$), in which the MUSE data for each galaxy has been binned to $\sim 500 \text{ pc}$ per spaxel and then refit with `THREADCOUNT`. The first binning scheme, 3×3 , simply restructures the cubes to match seeing, while the coarser binning, to 500 pc, is intended to increase S/N of line measurements and probe the lowest surface brightness more robustly. In all maps, we observe $\text{H}\alpha$ flux decreasing with height from the midplane, whilst $\text{H}\alpha$ velocity dispersion and $[\text{NII}]/\text{H}\alpha$ generally increase.

3.1 $\text{H}\alpha$ Morphology

Fig. 3 shows we observe $\text{H}\alpha$ emission at heights greater than $\pm 4 \text{ kpc}$ in all but one target, NGC 3957. This galaxy possesses both the lowest SFR and lowest extraplanar $\text{H}\alpha$ surface brightness in our sample. All targets with $\text{SFR} \geq 1 \text{ M}_\odot \text{ yr}^{-1}$ have extended $\text{H}\alpha$ emission. We will discuss correlations of the extended emission with galaxy SFR in later sections of this paper.

Many galaxies in our sample show filamentary substructures in the $\text{H}\alpha$ flux, which extend at near-to-perpendicular angles from the disk midplane outward into the extraplanar regions. We see these features in ESO 484-036, NGC 4666, NGC 5775, ESO 079-003, IC 1711, UGC 00903, ESO 120-016. Comparable features in NGC 3279 do not extend as far. Such substructure has likewise been discussed in M 82 using JWST ([Fisher et al. 2025](#)) and HST $\text{H}\alpha$ imaging ([Lopez et al. 2025](#)). This suggests similarity of GECKOS outflows to M 82.

NGC 4666 is described in [Mazzilli Ciraulo et al. \(2025\)](#) to show the traditional biconical structure, which the MUSE FOV here shows part. Similarly NGC 5775 has been shown to have a biconical wind ([Heald et al. 2006, 2022](#)), of which a portion is covered. ESO 484-036 is shown in [Veilleux & Rupke \(2002\)](#) to likewise show biconical structure, which is visible in the figure. We report that ESO 079-003 shows biconical filaments in $\text{H}\alpha$ flux that are consistent with the traditional bicone morphology.

NGC 3957, the lowest SFR galaxy in our sample ($0.3 \text{ M}_\odot \text{ yr}^{-1}$), has an off-center filament of gas extending over $\sim 2 \text{ kpc}$ from the disk. This is dissimilar to the extraplanar emission in other GECKOS targets, and that observed in low SFR systems with MUSE (e.g. [González-Díaz et al. 2024](#)). Like all other targets in this sample, the $\text{H}\alpha$ surface brightness of NGC 3957 peaks at the galactic center. We check that WISE W3 shows a similar central peak, which gives an SFR indicator that is more robust to extinction. The off-center filament in NGC 3957 is not connecting to the strongest star formation in the galaxy, but instead to a relatively lower SFR region of the disk. Moreover, the kinematics of this filament are irregular. As shown in the rightmost panel of Fig. 3.1, the gas at -1 kpc below the midplane is counter-rotating with respect to the disk at the same major-axis position. This feature sets this off-center plume apart from other filaments in our sample.

3.2 Velocity Dispersion Maps

In all targets the velocity dispersion increases at greater vertical distance from the midplane. In several galaxies (e.g. ESO 484-36 and ESO 079-003) the elevated velocity dispersion has a biconical

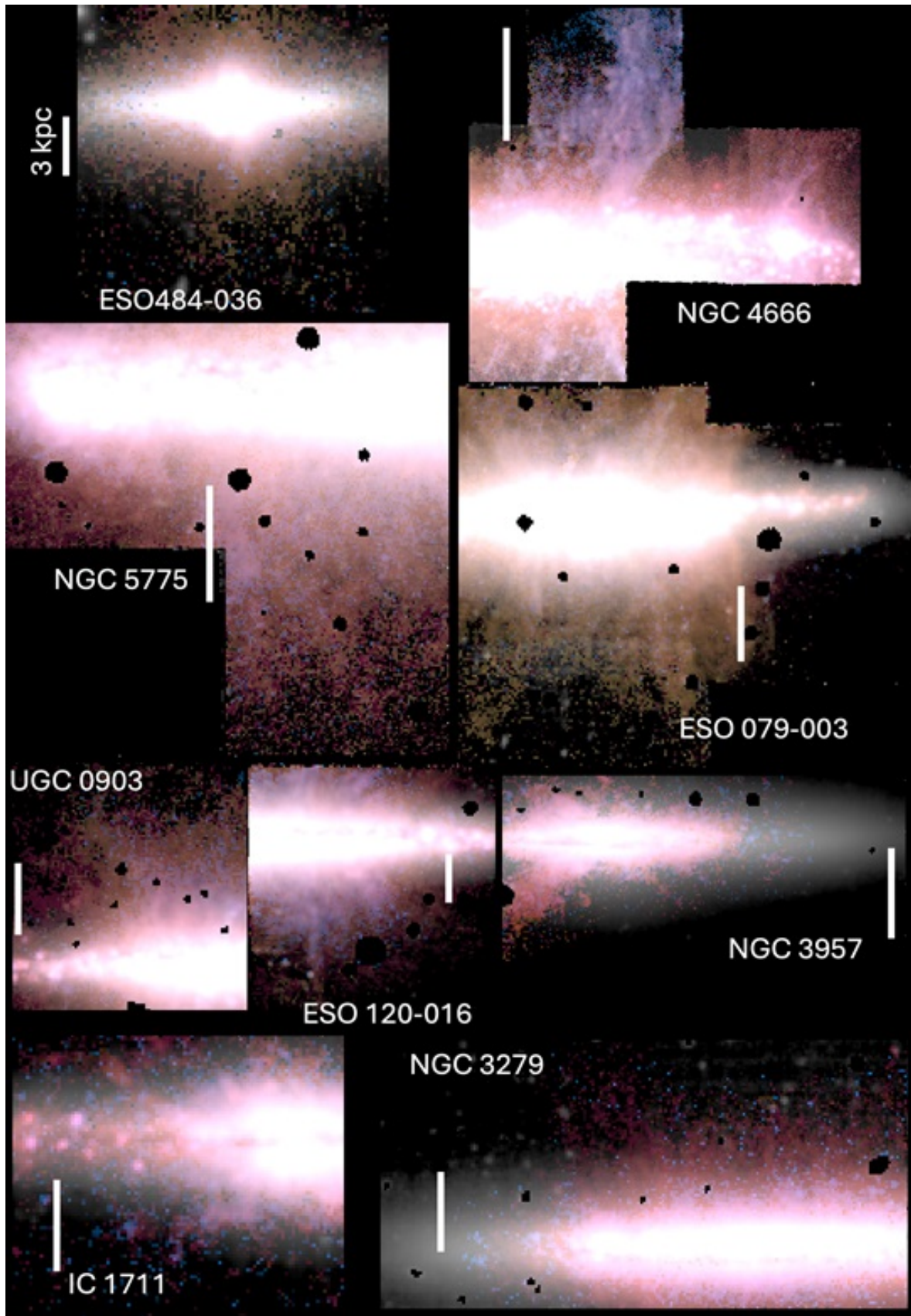


Figure 2. Four colour emission line plus continuum images of GECKOS targets studied in this paper. In all figures, H α emission is shown in red, [NII] 6583 in yellow, [OIII] 5007 in blue, and R band continuum in white. The white line in each panel represents a ~ 3 kpc scale. Extraplanar emission is visible in all targets, often forming multi-kiloparsec filaments extending out from the disk.

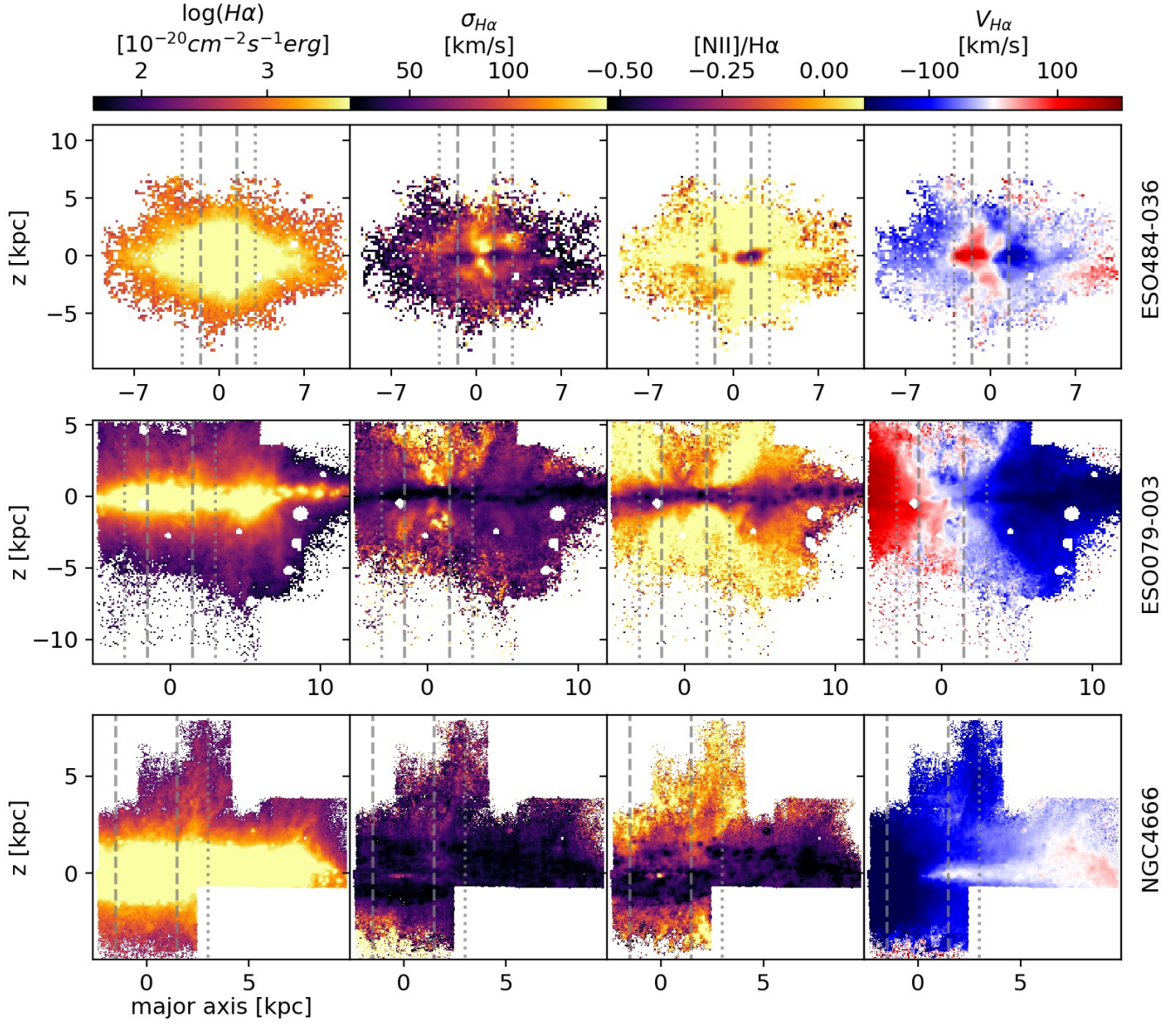


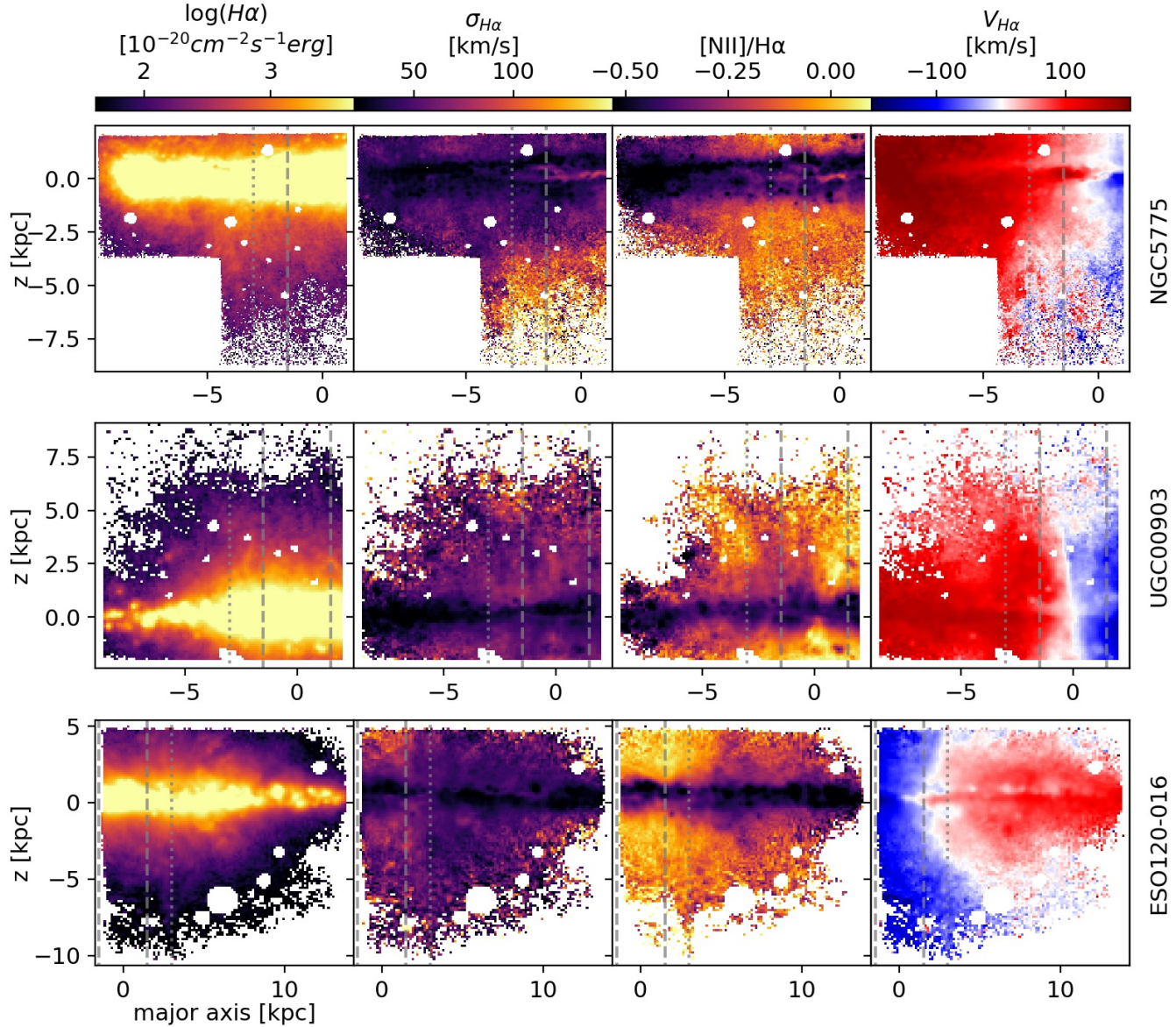
Figure 3. Maps of $\log(H\alpha)$ flux (left), $H\alpha$ velocity dispersion that has been corrected for instrumental dispersion (middle-left), and $\log([NII]/H\alpha)$ flux ratio (middle-right) and velocity (right) made for each galaxy in our sample. Note that the galaxies in this figure are ordered by decreasing SFR. Spatial axes are in units of kpc. The points where the vertical and horizontal axes equal 0 kpc mark the approximate location of the galactic midplane and rotational center respectively. We mark the 1.5 kpc and 3.5 kpc points on the major axis with vertical gray dashed and dotted lines respectively.

shape over the center of the galaxy. For this analysis, we include discussion of the 500 pc resolution dispersion maps in Fig. 4. The 500 pc maps allow us to probe further from the galaxy center, albeit at a $\sim 2.5 - 10 \times$ coarser resolution than the 0.6 arcsec resolution maps in Fig. 3. We remind the reader that the instrumental dispersion is subtracted in quadrature from the fitted dispersion.

We also note for physical interpretation of $\sigma_{H\alpha}$ that in extraplanar gas the velocity dispersion may not indicate turbulence, especially at MUSE spectral resolution. McPherson et al. (2023) describe how the line-of-sight expansion of a bicone when convolved with relatively low spectral resolution ($R \lesssim 3000$) could appear as a broadened line rather than line-splitting. We will consider this in the text when appropriate.

We first consider galaxies with higher SFR $\gtrsim 5 M_\odot \text{ yr}^{-1}$. Galaxies

ESO 484-036, NGC 5775 and ESO079-003 show extensive extraplanar regions with $\sigma_{H\alpha} > 100 \text{ km s}^{-1}$ that is above $z \gtrsim 1 \text{ kpc}$ and within 1 kpc of the major-axis center. In ESO 079-003, the high dispersion regions form a triangular structure that extends up to $\sim 10 \text{ kpc}$ from the galaxy midplane. This structure is visible in both the 0.6 arcsec resolution maps (Fig. 3) and 500 pc resolution maps (Fig. 4). At a constant height of $z \sim 1 \text{ kpc}$, the velocity dispersion drops to values of $\sim 40 - 60 \text{ km s}^{-1}$ outside this triangular region. A similar triangular region may be present in ESO 484-036, as can be seen most clearly in the 500 pc maps (Fig. 4). We cannot fully describe the morphology for NGC 5775; this is because the extraplanar MUSE pointings do not cover the entire outflow, and only extend $\sim 5 \text{ kpc}$ from the galaxy center (on the major-axis). We do, however, identify high dispersion gas ($\sigma_{H\alpha} > 100 \text{ km s}^{-1}$) above the galactic center of NGC 5775, which

Figure 3 – *continued*

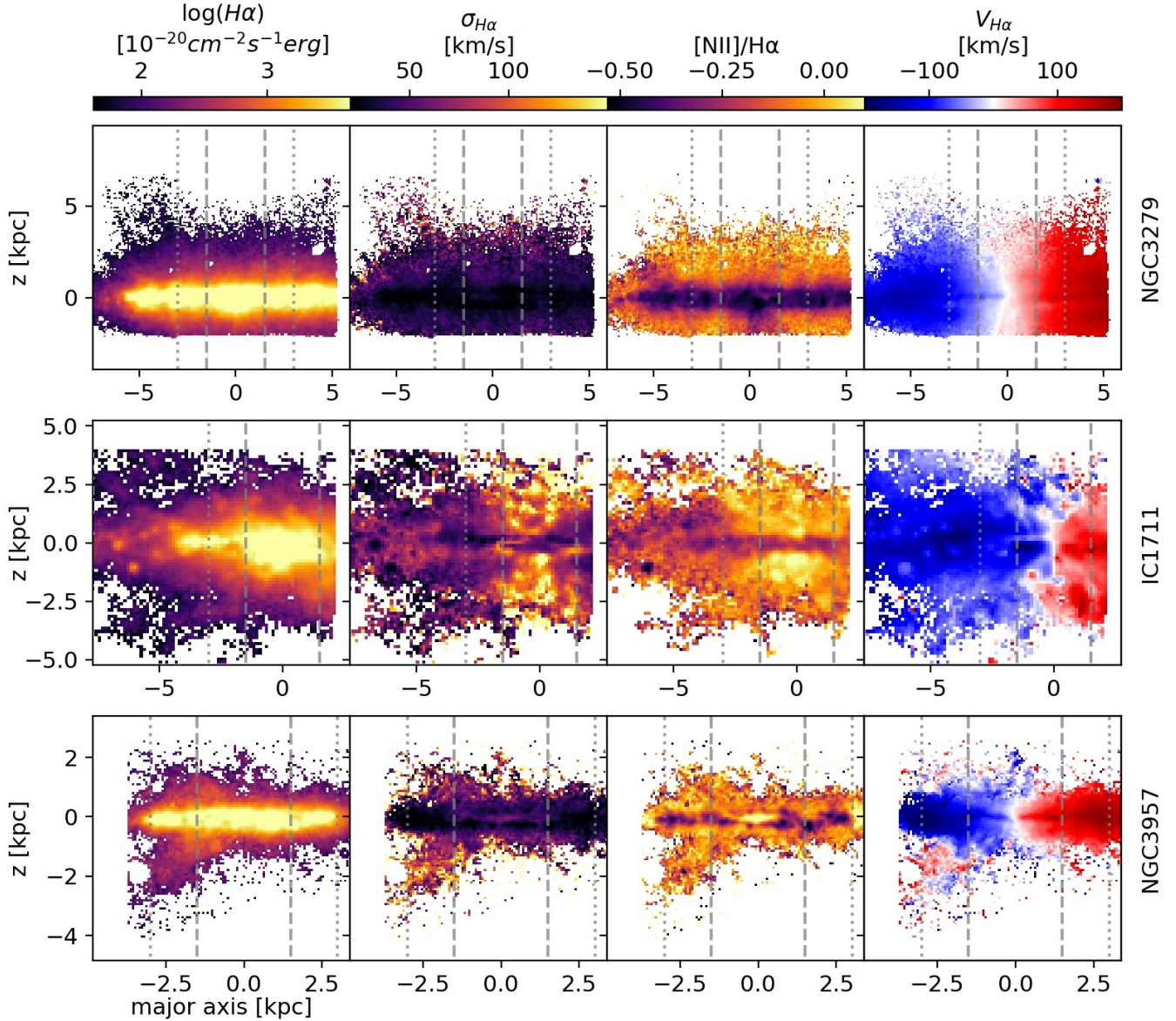
declines near the edge of the field-of-view at ~ 4 kpc from the major axis center. NGC 4666 shows a strong rise in $\sigma_{H\alpha}$ on the lower side of the 500 pc map, but limited spatial coverage obscures the shape of this $\sigma_{H\alpha}$ enhancement. Likewise on the top side of NGC 4666, the coverage barely includes the center of the major-axis in the wind region, which means that detecting a centrally located rise in $\sigma_{H\alpha}$ is difficult. Overall, in the high SFR super-main sequence systems with sufficient spatial coverage, there is evidence of a biconical high dispersion structure in the 500 pc resolution velocity maps.

We now consider the lower SFR galaxies. UGC 00903 and ESO 120-016 also have elevated dispersions in extraplanar gas above the disk center (on the major-axis), which have peak values of $\sigma_{H\alpha} \sim 70$ km s $^{-1}$. Higher SFR systems commonly reach $\sigma_{H\alpha} \sim 100$ –150 km s $^{-1}$, which can be twice the highest values in most of the low SFR systems. Fig. 4 also displays $\sigma_{H\alpha} > 100$ km s $^{-1}$ regions above the planes of NGC 3957 and NGC 3279, but these do not

share the triangular shapes seen in galaxies like ESO 079-003 and ESO 484-036.

IC 1711 displays a high dispersion triangular region. Unlike other galaxies with this feature, IC 1711 has a modest SFR ($\sim 1 M_\odot \text{ yr}^{-1}$) and little $H\alpha$ emission beyond a minor axis height ~ 4 kpc. One interpretation is that IC 1711 could contain historic wind activity. Simulations show this could leave a mark on the extraplanar gas (see Pillepich et al. 2021). This activity could be from alternate possibilities, such as a weak AGN that is currently driving a low mass outflow. We discuss the case of IC 1711 in more detail later.

McPherson et al. (2023) discuss the use of velocity dispersion in extraplanar emission as a diagnostic for galactic winds, separating it from extraplanar emission not associated with the wind. Similar conclusions can be drawn from inspection of outflows discussed in Bik et al. (2018) and Watts et al. (2024). McPherson et al. (2023) argue that high dispersion signatures are generated by the expansion of a biconical structure in ionised gas, which, when observed with modest

Figure 3 – *continued*

spectral resolution ($R \sim 2000 - 3000$), appears as a broad Gaussian emission line. Turbulence generated within the outflow would further increase this velocity dispersion. Our velocity dispersion results are consistent with this, albeit with some caveats. ESO 484-036, NGC 4666, NGC 5775 and ESO 079-003 all have $\text{SFR} \geq 5 \text{ M}_\odot \text{ yr}^{-1}$, and the first 3 of these galaxies have known outflows (Veilleux et al. 2005; Hearn et al. 2006). NGC 5775 and NGC 4666 have limited MUSE coverage of the wind, making it difficult to identify any biconical dispersion structures. However, the 500 pc image does show high dispersion values on the lower side of NGC 4666, as well as increased dispersion around $z \sim 5 - 7 \text{ kpc}$ on the top side. We see likewise for $z < 4 \text{ kpc}$ in NGC 5775. These high dispersion values may trace some triangular dispersion structures, but we cannot be certain without a wider field-of-view.

These first results from GECKOS galactic winds, especially in Fig. 4, allow us to create more formalized criteria for outflows. We rely on the assumption that at the same stellar mass, galaxies with

higher SFR are expected to be more likely to have strong outflows (e.g. Heckman et al. 2015; Chisholm et al. 2015; Veilleux et al. 2020b; Thompson & Heckman 2024). More specifically in our sample, the literature has described our high SFR systems as having outflows (see references above). We then interpret that our galaxies with $\text{SFR} \geq 5 \text{ M}_\odot \text{ yr}^{-1}$ are outflow systems. Under this assumption we find the following:

(1) **Elevated Velocity Dispersion as an Outflow Identifier:** We find that when the velocity dispersion of the outflow is above $\sim 100 \text{ km s}^{-1}$ this system is most likely a stronger, biconical outflow. We note that, as seen in other works, we observe at least some increase in velocity dispersion with increasing distance from the midplane for all galaxies in our sample, but the outflow systems have a larger increase.

(2) **Velocity Dispersion Morphology as an Outflow Identifier:** We find that there is a triangular/biconical morphology in $\sigma_{\text{H}\alpha}$ above most high-SFR galaxies. Our results are therefore consistent with previous arguments that biconical morphology in a velocity disper-

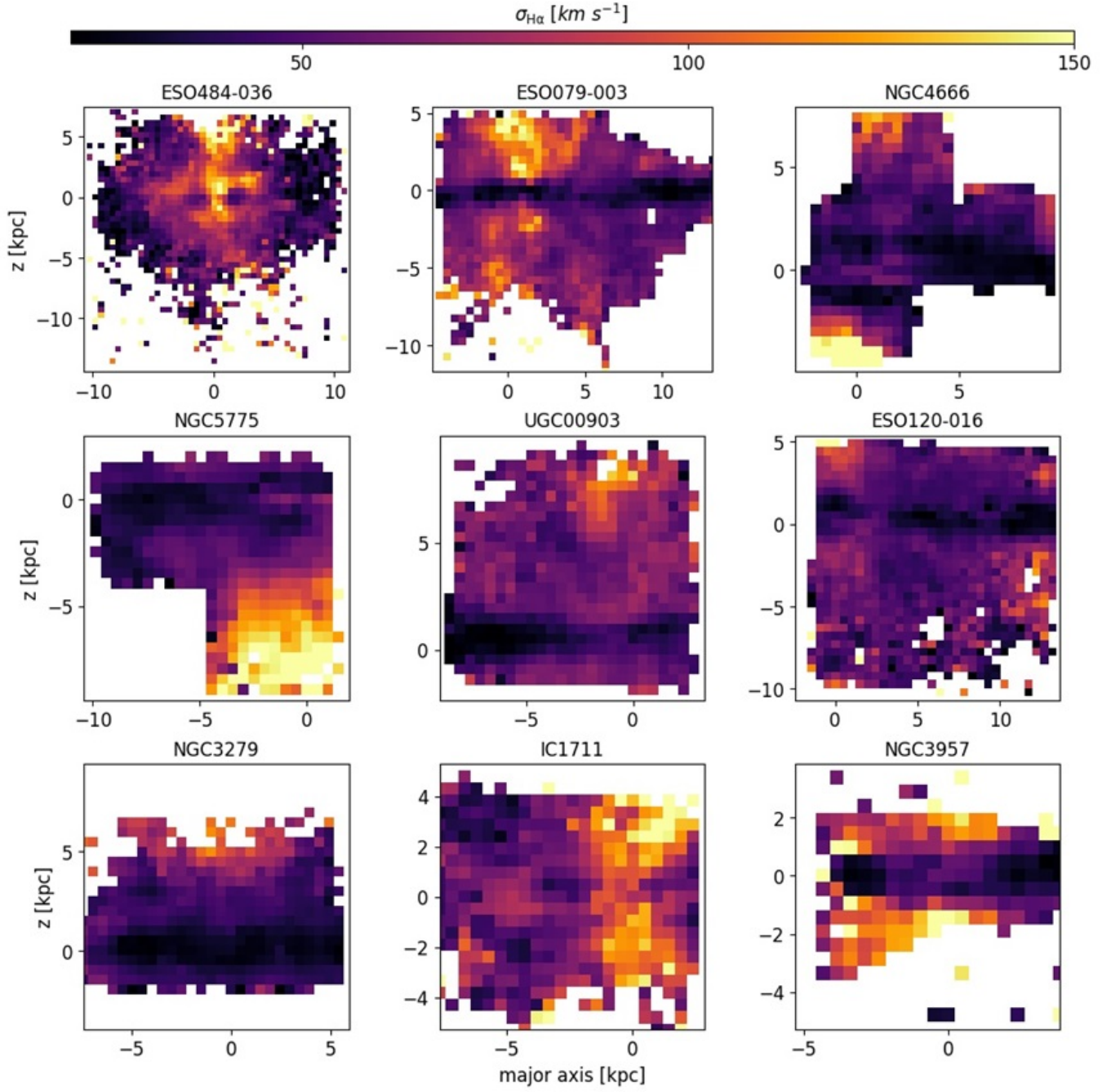


Figure 4. H α velocity dispersion maps made from 500 pc resolution data for each galaxy. The points where the vertical and horizontal axes =0 mark the approximate location of the galactic midplane and rotational axis respectively.

sion map appears to be a good indicator that this gas is associated to a strong biconical outflow (e.g. McPherson et al. 2023). We add the caveat that some galaxies with such morphology, as found in IC 1711, are not fully understood and may have an alternative origin.

3.3 Ionization Morphology

The [NII]/H α maps, shown in the 3rd column of Fig. 3, of each galaxy allow us to visualise the morphology of the ionisation in the extraplanar gas. The classic ‘X-shape’ structure in this emission line

ratio, where arms of the X extend outward from the galaxy centre, has been described as indicative outflows for many years (e.g. Veilleux et al. 2005). This is most clear in ESO 079-003, which shows higher levels of [NII]/H α in the limbs of the outflow. Though we note that in this target the bright H α knot located at roughly \sim 6–7 kpc on the major-axis has a low [NII]/H α , and is not part of the high-ionisation X-shape. In ESO 484-036, ESO 079-003, IC 1711, UGC 00903 and ESO 120-016, [NII]/H α peaks above the galaxy center (seen within major axis cuts of 1–2 kpc). As with velocity dispersion, it is difficult to interpret [NII]/H α in NGC 4666 and NGC 5775 due to the limited

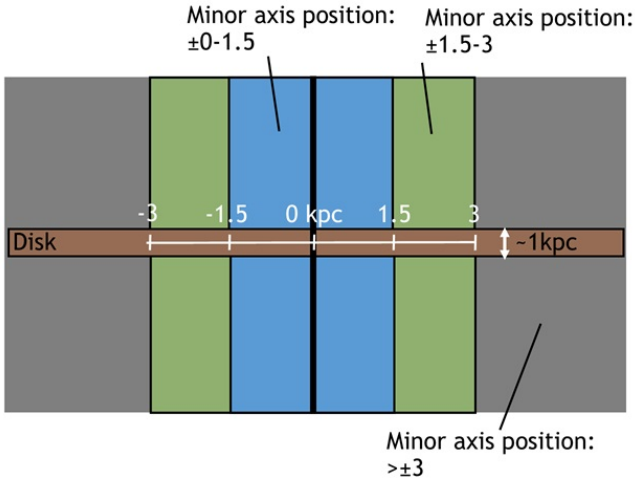


Figure 5. Illustration of the regions defined for each galaxy in this paper. Brown highlights the disk region, blue highlights the “major axis: $\pm 0-1.5$ kpc” region, green highlights the “major axis: $\pm 1.5-3$ kpc” region, and the grey area outside of these highlights is the “major axis: $> \pm 3$ kpc” region. When we project these regions onto an observation of an edge-on galaxy, the “disk” region aligns with the galactic midplane, and the “0 kpc” mark aligns with the galactic center.

field-of-view coverage. We note that the morphologies of [NII]/H α of two of the lower SFR targets (NGC 3279 and NGC 3957) differ strongly from higher SFR galaxies like ESO 079-003.

We note again the difference of IC 1711 to other low-SFR systems. IC 1711 has the second lowest SFR in our target list, yet the morphology of the [NII]/H α ratio more suggests a high ionization cone above the galaxy center. This again suggests the possibility for an alternate source of the extraplanar emission, as discussed above and will be discussed below in the Discussion.

3.4 Regions of Extraplanar and Disk Emission

For our analysis of the ionised gas emission line ratios, we divide each galaxy into four empirically selected regions. These regions are motivated by previous observations of outflows, where hotter, more ionized gas is expected over the galaxy center and cooler/lower ionisation gas is found at further distances along the major axis (Shopbell & Bland-Hawthorn 1998a; Veilleux et al. 2005; López-Cobá et al. 2020; Veilleux et al. 2020b). Our sample, which includes a range in SFR and likely a range in galactic wind strength, can empirically determine if this structure is connected to the presence of stronger winds. We illustrate the regional separations, described below, in Figure 5. The *disk* region is designed to align with the midplane of the galaxy, and capture ionization in the disk. It is not meant to include extraplanar emission. We define a 1 kpc thick region that extends along the full major-axis of the galaxy. This thickness is similar to the size of regions described as disk in previous outflow studies (e.g. McPherson et al. 2023). The extraplanar emission is divided into 3 regions based on the distance to the major-axis galaxy center. The boundaries for these separations based on *ad hoc* inspection of Fig. 3, with special emphasis on the velocity dispersion. Based on what we have already discussed, we therefore expect a decrease in [NII]/H α and $\sigma_{H\alpha}$ moving from the regions above the galaxy center towards those horizontally offset from the prior region. These definitions are intended to help us better quantify this decrease.

3.5 Vertical H α surface brightness profiles

Figure 6 shows vertical profiles of H α surface brightness, $\Sigma_{H\alpha}$, for each galaxy. We make profiles using 0.6 arcsec resolution data (top row) and 500 pc resolution data (bottom row). Profiles are generated with the average of $\Sigma_{H\alpha}$ in each row, within each subregion, and restricting the averages to only include $S/N > 5$ on the emission line in individual spaxels. In all profiles the central ± 500 pc, the disk region discussed above, is omitted. The profiles, therefore, concentrate on extraplanar emission only.

In Fig. 6 there is a trend that highest SFR galaxies have high surface brightness $\Sigma_{H\alpha}$ profiles, and lowest SFR galaxies have lowest surface brightness profiles. This is most clear for the left and center panels, which represent emission closer to the galaxy center (on the major-axis). In the left-hand panels, galaxies ESO 484-036, NGC 4666, NGC 5775, ESO 079-003, ESO 120-016, and UGC 00903 exhibit emission extending up to ~ 5 kpc from their midplanes. In contrast, the lowest SFR galaxies (NGC 3957, NGC 3279, and IC 1711) only reach $\sim 2-3$ kpc above the midplane. Assuming that H α flux is a mass tracer, and that gas generating extraplanar emission originates in the galaxy there are many reasons why we would expect the low SFR systems to have less extended profiles of H α emission.

It is interesting to note that IC 1711 has a low $\Sigma_{H\alpha}$ values, that do not extend as far as the high SFR galaxies. We have discussed how the kinematics and emission line ratios of IC 1711 were more similar to high-SFR galaxies, yet this similarity does not extend to the H α brightness. If one assumes that the biconical shape to the $\sigma_{H\alpha}$ on this galaxy suggests an outflow, then the H α surface brightness would suggest a very low mass in the outflow of IC 1711.

4 EMISSION LINE RATIO DIAGNOSTICS OF IONISATION MECHANISMS

The Baldwin–Phillips–Terlevich (BPT) diagram (Baldwin et al. 1981) is a widely used tool to investigate the ionization mechanism driving emission line fluxes (reviewed in Kewley et al. 2019b). IFU studies have further applied BPTs to prove spatial variation in ionisation across various star-forming galaxies (e.g. Ho et al. 2014; Davies et al. 2014; Sharp & Bland-Hawthorn 2010; Sánchez 2020).

In this section, we create BPT diagrams to study the ionisation properties of extraplanar gas in our sample. We will use these diagrams to compare galaxies and galaxy regions (defined in Section 3.4) in our sample. We will also use these diagrams to check differences between galaxies that are higher SFR galaxies than from lower. In resolved studies of face-on galaxies, Reichardt Chu et al. (2025) finds that outflows are more common for specific star formation rate, $SFR/M_{star} > 0.1 \text{ Gyr}^{-1}$. For a galaxy with, $M_\star \sim 5 \times 10^{10} \text{ M}_\odot$ (median GECKOS stellar mass), $SFR/M_{star} \sim 0.1 \text{ Gyr}^{-1}$ corresponds to $SFR \sim 5 \text{ M}_\odot \text{ yr}^{-1}$.

In this study, we construct two types of emission line ratio diagrams for each galaxy: [NII]/H α against [OIII]/H β ; and [SII]/H α against $\sigma_{H\alpha}$. As a test, we created BPT diagrams of [SII]/H α against [OIII]/H β to identify AGN activity signatures in our line-ratio data. Though these extra BPT diagrams are not shown in this paper, we did not find clear AGN signatures using [SII] in place of [NII]. In each diagram, we only include pixels with $S/N > 5$ detections for [NII], H α , [OIII], and H β .

Traditionally, BPT diagrams use theoretical classification curves (e.g. Kewley et al. 2001; Kauffmann et al. 2003) that define regions of the parameter space dominated by different ionisation mechanisms. However, the shape and position of these curves depend on the hardness of the local ionizing radiation field (Kewley et al. 2019a). We

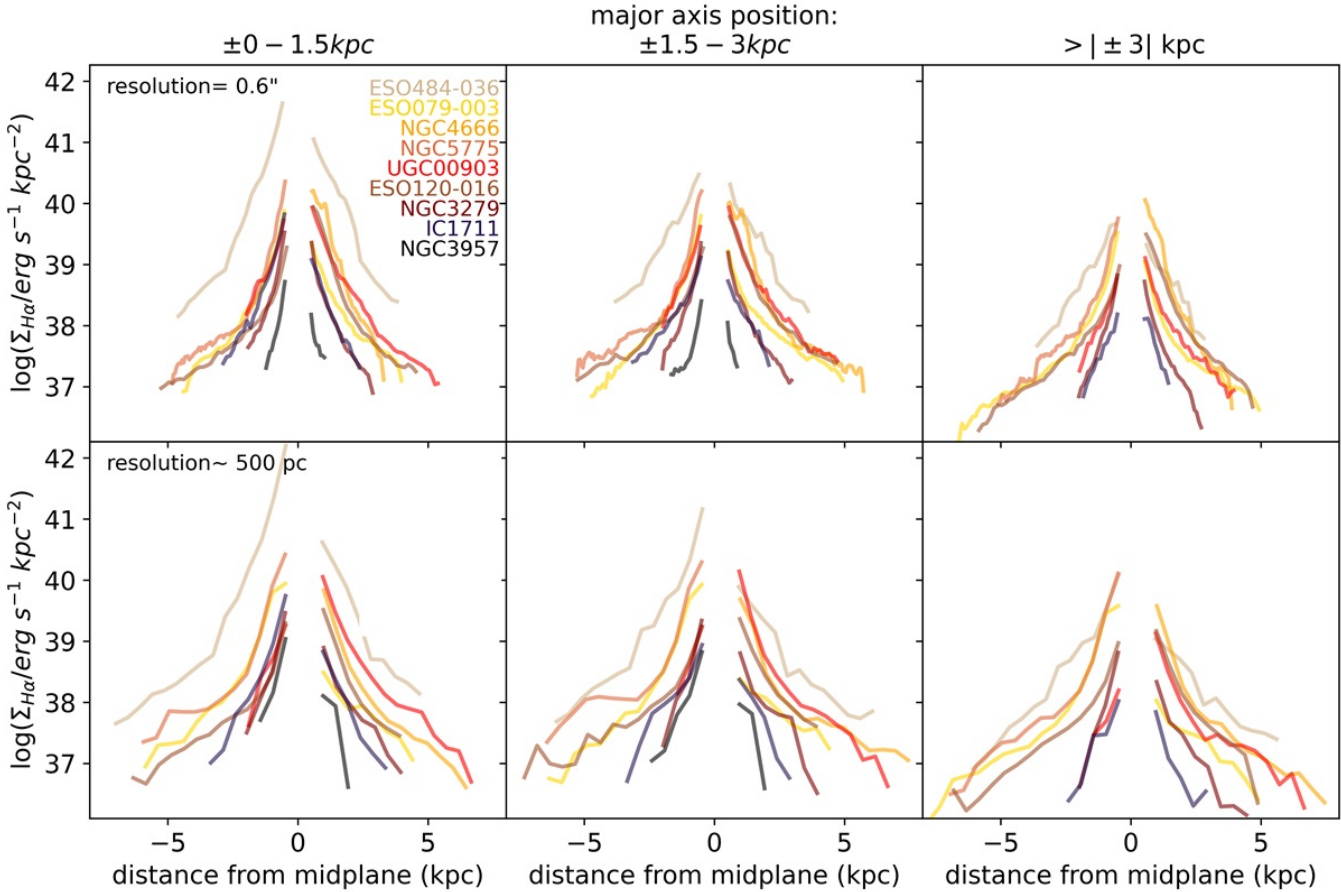


Figure 6. Vertical $H\alpha$ surface brightness profiles. Row 1 shows profiles made from 0.6 arcsec resolution data (i.e.: the same resolution shown in Fig. 3), and row 2 shows profiles made from 500 pc resolution data. Each column displays profiles made from the 3 extraplanar regions defined in Section 3.4 (see Fig. 5). For NGC 4666 and NGC 5775, only one side of their minor axis profile is displayed, due to the vertically limited field of view for these galaxies. Galaxies in the legend are listed in the order of decreasing SFR. Galaxy centers ± 500 pc are omitted to better emphasize the extraplanar gas.

must consider this effect for our galaxy sample, as we expect harder radiation fields to occur naturally in lower attenuated extraplanar regions. To account for varying ionizing field strengths, we use the variable classification curve by equation 5 of Kewley et al. (2013) in our $[NII]/H\alpha$ against $[OIII]/H\beta$ BPT diagrams. We, therefore, plot two curves, that with smaller line ratios represents the standard star forming sequence from Kewley et al. (2013); the solid curve with larger line ratios represents a harder field.

Fig. 7 shows 2D contours of the $[NII]/H\alpha$ - $[OIII]/H\beta$ diagram for our targets. The contours represent kernel density estimates of the distribution of pixels from corresponding galaxies. We show levels that include 66% and 99% of the probability mass for each contour set. We separate the galaxies into the following three subsets: $SFR \geq 5 M_\odot \text{ yr}^{-1}$ galaxies (blue contours), $SFR < 5 M_\odot \text{ yr}^{-1}$ galaxies (red contours) and IC 1711 (green contours). We have separated IC 1711 due to the differences in morphology of both $\sigma_{H\alpha}$ and ionization maps described in the previous sections. Each subplot displays a shock model grid (black dashed line) and two thermal ionization models (solid lines). The shock models taken from Tables 6 and 8 of the MAPPINGSIII simulation paper by Allen et al. (2008). Thermal emission models are generated using equation 5 in Kewley et al. (2013). The region between these shocks and thermal emission is often described as the “mixing sequence”, where the relative contributions of thermal and non-thermal ionization are ambiguous. We

show $[NII]/H\alpha$ - $[OIII]/H\beta$ diagrams for all individual targets in the Appendix. Figures in the appendix show individual spaxels, which are colored by distance to the galaxy midplane.

4.1 Line ratios for extraplanar gas of high SFR galaxies

We now examine emission line diagnostics for galaxies with $SFR \geq 5 M_\odot \text{ yr}^{-1}$, indicated as the blue lines in Fig. 7 and Fig. 8. This group consists of ESO 484-036, NGC 4666, NGC 5775, and ESO 079-003, each shown independently in Appendix Figs. A1, A2, A3 and A4. The first three of these targets have known outflows (Veilleux et al. 2005; Dahlem et al. 1997; Heald et al. 2006). ESO 079-003 exhibits a pronounced X-shape structure in $[NII]/H\alpha$ (Fig. 3), a high velocity dispersion cone structure (Fig. 3 and Fig. 4), and very extended $H\alpha$ emission (Fig. 6). ESO 079-003 is therefore consistent with several indicators of having a strong galactic wind. Therefore, we interpret this group as a sample of outflow-dominated systems.

The blue contours in the top two panels of Fig. 7 both show emission line ratios for the $SFR \geq 5 M_\odot \text{ yr}^{-1}$ galaxies that extend beyond the thermally excited regime and into the non-thermal regime, consistent with shocks ($v_{\text{shock}} \sim 200 - 300 \text{ km s}^{-1}$). This includes both the region designed to cover the central part of the outflow (± 0 - 1.5 kpc) and the region that covers the edge of the outflow (± 1.5 - 3.0 kpc). The plots in the Appendix show that there is a correlation

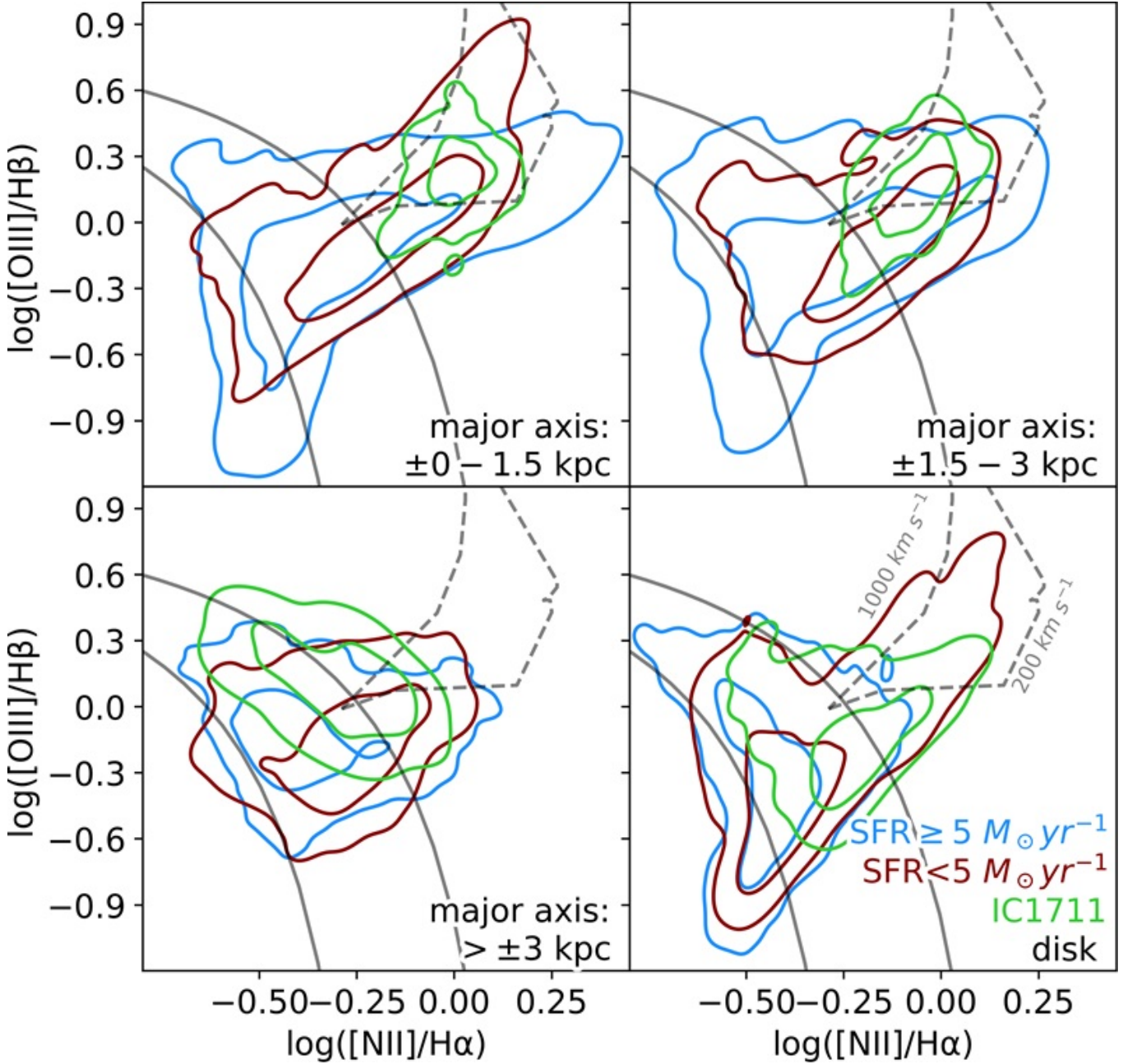


Figure 7. A set of $[\text{NII}]/\text{H}\alpha$ against $[\text{OIII}]/\text{H}\beta$ 2D histograms, combining all pixels with $S/N > 7$ in each line from our sample. We divide the sample into galaxies with $\text{SFR} \geq 5 \text{ M}_\odot \text{ yr}^{-1}$ (blue contours), IC 1711 (green contours) and those with SFR below this (red contours). Contours represent the top 66% and 99% of pixels in each category. Separate BPT diagrams are shown for the 4 galaxy regions defined in Section 3.4 (see Fig. 5). The spacing of the two solid lines reflect an increasing radiation-field, with the line for larger line ratios representing the harder field (Kewley et al. 2013). The black dashed line represents a shock model grid from MAPPINGSIII simulations (Allen et al. 2008), covering shock velocities between 200 km s^{-1} and 1000 km s^{-1} , which represent the boundaries of available models.

of larger values of emission line ratios (especially $[\text{NII}]/\text{H}\alpha$) with distance to from the galaxy midplane. We note that the majority of spaxels fall outside the region occupied by the Allen et al. (2008) shock models.

For the positions more distant from the galaxy center (major-axis position $> 3 \text{ kpc}$) the majority of spaxels are consistent with thermal emission. There is only a small spur of gas that extends along the mixing sequence, albeit with lower $[\text{OIII}]/\text{H}\beta$ than observed in the central regions of the extraplanar gas. These results are consistent

with differences in ionisation near to (above) the galaxy center, with decrease strength in ionisation for gas more distant to the center of the galaxy.

Fig. 8 compares $[\text{SII}]/\text{H}\alpha$ to the $\text{H}\alpha$ line velocity dispersion for our $\text{SFR} \geq 5 \text{ M}_\odot \text{ yr}^{-1}$ galaxies (blue contours). We do not include ESO 484-036 in this figure, due to a skyline overlapping with $[\text{SII}]$. The highest velocity dispersions are found in the regions above the galaxy centers ($\pm 0-1.5 \text{ kpc}$), reaching $\sigma_{\text{H}\alpha} \sim 150 \text{ km s}^{-1}$. In all extraplanar regions, $\sigma_{\text{H}\alpha}$ positively correlates with $[\text{SII}]/\text{H}\alpha$ for $\sigma_{\text{H}\alpha} \lesssim 60 -$

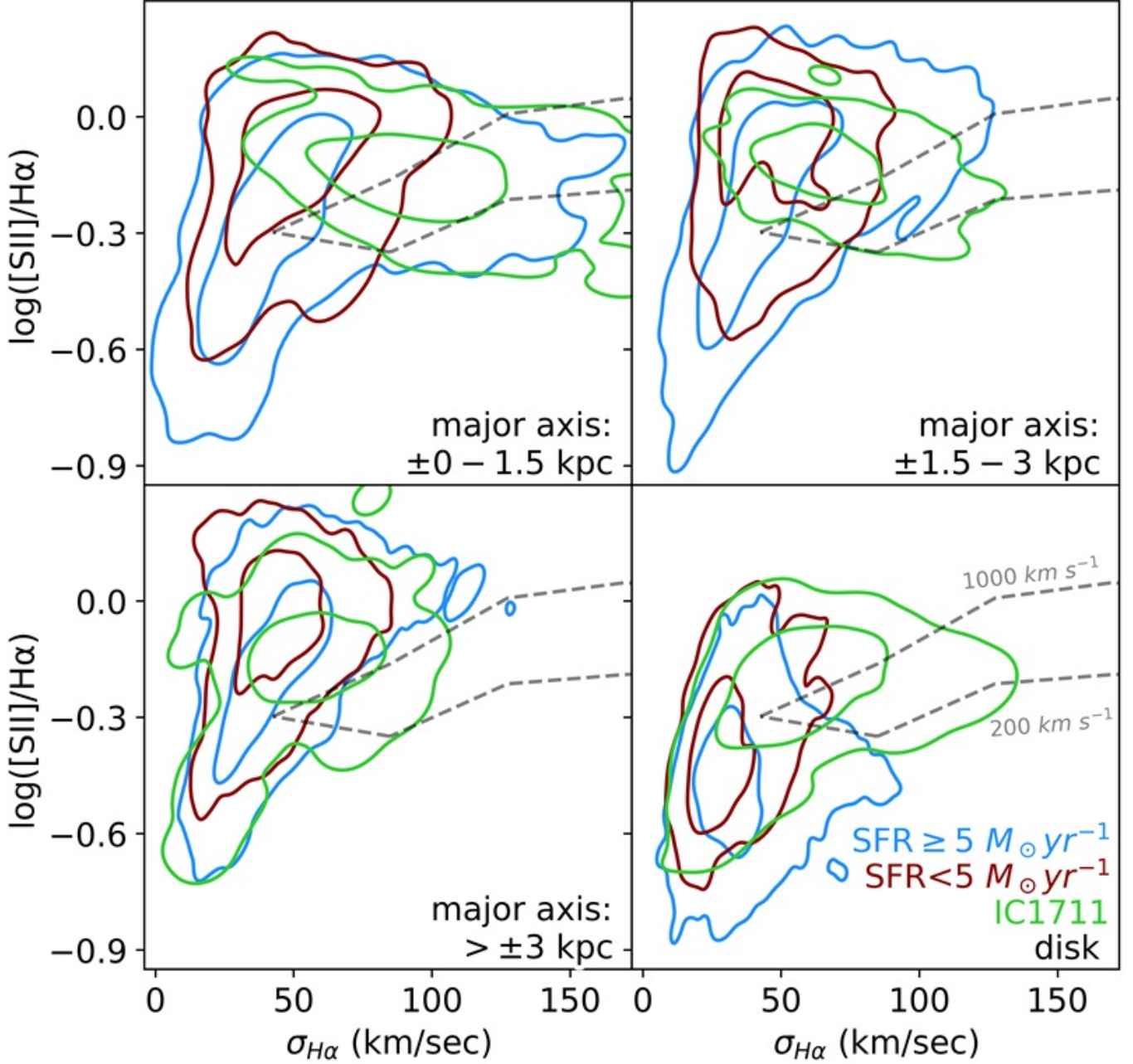


Figure 8. Similar galaxy groups as shown in Fig. 7, here plotting $\sigma_{H\alpha}$ against $\log([SII]/H\alpha)$. These diagrams follow the same general structure as Fig. 7.

70 km s^{-1} . This corresponds to $[SII]/H\alpha \sim 1$. For larger velocity dispersions ($\sigma_{H\alpha} \sim 80-150$ km s^{-1}) there is not significant increase in $[SII]/H\alpha$.

Kewley et al. (2019b) argue that shocks are probable drivers of emission line if (1) shock-sensitive line ratios, such as $[SII]/H\alpha$, correlate with dispersion, and (2) the velocity dispersion is larger than ~ 80 km s^{-1} . We find a mixture of evidence for shocks in gas above the plane in the GECKOS high SFR targets. We, likewise, point out that only a small fraction of spaxels show both high $\sigma_{H\alpha}$ and a positive correlation between $\sigma_{H\alpha}$ and $[SII]/H\alpha$. Additionally, Fig. 7 shows that the most elevated line ratios remain near to the lower end of the Allen et al. (2008) shock model grid. This may be due to the models being designed for ISM conditions, rather than outflows.

Alternatively, shock fronts likely occur on much smaller scales than our spatial resolution (50–200 pc). Recent work finds that clouds are typically on the order of 10 pc in width (Fisher et al. 2025). If shocks occur on these scales, and are embedded in a non-shocked gas, then our observations would blend the two together. This could modify the measured emission line ratio.

Chisholm et al. (2017) finds negligible contribution of shocks from UV absorption lines in outflows, though it is important to note that absorption lines and emission lines do not trace gas in the same way. Nevertheless, the lack of difference in the nature of the $[SII]/H\alpha - \sigma_{H\alpha}$ relationship, and relatively few spaxels that overlap with shock models, may simply reflect a minimal role of shocks in the ionization of wind gas.

McPherson et al. (2023) discusses the observational effect for observing outflows with relatively low spectral resolution instruments ($R \sim 1000 - 3000$), like MUSE. Observations of nearby outflows with higher spectral resolution observe split emission lines in outflows (Westmoquette et al. 2008, 2011). The line-splitting is understood to result from the two sides of an expanding cone of gas. If an expanding cone is observed with lower spectral resolution, this would appear as higher velocity dispersion for a single Gaussian component. An interpretation of the shape of the $[SII]/H\alpha - \sigma_{H\alpha}$ relationship could be that at low dispersion there is a physical link between the ionisation and gas kinematics, but at higher velocity dispersion the velocity dispersion reflects the expanding cone, which is unrelated to the ionisation mechanism.

4.2 Line ratios for extraplanar gas of main-sequence galaxies

In Fig. 7 we also show the 66% and 99% contours of the $[NII]/H\alpha$ - $[OIII]/H\beta$ values for galaxies with $SFR < 5 M_\odot \text{ yr}^{-1}$ (i.e. ESO 120-016, NGC 3279, NGC 3957, UGC 00903), excluding IC 1711. The lower SFR systems are shown as red contours. These galaxies lie within ± 0.3 dex of the main-sequence SFR for their given mass, with lower SFR/M_* than is expected for strong outflows (see Table 1). We therefore interpret these galaxies as typical main-sequence star-forming galaxies in the local Universe, that are not typically associated to large-scale outflows.

The first thing we notice is that, in general, the contours for extraplanar gas of the low- and high-SFR occupy similar regions of $[NII]/H\alpha$ - $[OIII]/H\beta$ parameter space. The majority of spaxels, indicated by the inner 66 percentile contours, of both subsets of galaxies overlap well. While the distributions are similar, there are subtle differences between the distribution of extraplanar gas in the $[NII]/H\alpha$ - $[OIII]/H\beta$ diagram for high and low SFR galaxies. The high SFR systems reach ratios of $[NII]/H\alpha \sim 3$, while the main-sequence systems are rarely far above $[NII]/H\alpha \gtrsim 1$. Conversely, the extraplanar emission of the main-sequence targets reach higher values of $[OIII]/H\beta$ (upper left panel) and a more substantial fraction of the spaxels fall in the shock model region.

In all 4 regions of the main-sequence galaxies (red contours), we find emission line ratios that extend from the thermal ionisation region of the BPT diagram, along the mixing sequence and into the region of the Allen et al. (2008) shock models. This is similar to the results of González-Díaz et al. (2024), who studies the extraplanar emission of 9 edge-on galaxies with SFR similar to the main-sequence targets of our sample. They find emission line ratios consistent with significant contribution from shocks.

The red contours in Fig. 8 show velocity dispersion- $[SII]/H\alpha$ distributions from galaxies with $SFR < 5 M_\odot \text{ yr}^{-1}$. Here the bulk of the low-SFR systems (all except IC 1711) have a very different relationship between $[SII]/H\alpha$ and $\sigma_{H\alpha}$ as compared to the high SFR systems. The low SFR systems cover a similar range of $[SII]/H\alpha$ but do not show the high velocity dispersion tail over the galaxy center that is present in the systems that are known to host strong outflows. This suggests that the differences in increased SFR do not impact the ionisation mechanism heavily, but do in fact lead to differences in the kinematics. This makes sense under the assumption that extraplanar gas is driven by feedback and that higher SFR have a larger mechanical energy in a launch mechanism. This larger energy generates a coherent biconical outflow. Conversely, feedback may drive gas above the plane in the main-sequence systems, but this does not form an expanding bicone.

The elevated values of $[NII]/H\alpha$ and $[OIII]/H\beta$ values in the disk region subplot of Fig. 7 correspond to NGC 3957 (see the Fig. A7).

This galaxy is different from the rest of the sample in many ways. Firstly, it has the least bright extraplanar gas. Secondly, the extraplanar gas that is present is located in an off-center plume that is counter-rotating with respect to the disk, and has elevated dispersion (see 2nd and 3rd column in Fig. 3.1 respectively). This counter-rotating plume is not typical for outflows, as outflowing material has often been shown to align closely with the galactic minor axis, and to co-rotate with the galactic disk (e.g. Shopbell & Bland-Hawthorn 1998b; Heald et al. 2006). An accretion or merger of a smaller galaxy could be consistent with counter-rotating, elevated gas. The merging gas does not need to have the same line ratios of the host, which could lead to this difference. Alternatively, Fig. 3 shows that the highest $[NII]/H\alpha$ values in NGC 3957 are associated to the galaxy center, possibly reflecting a contribution from AGN.

4.3 Emission line ratios for extraplanar gas in IC 1711

We have previously discussed the unique case, within our sample, of IC 1711. This galaxy has a low SFR, $\sim 1 M_\odot \text{ yr}^{-1}$, but the extraplanar gas shows a high dispersion cone-shape, which is more commonly found at high SFR. The $H\alpha$ surface brightness of the extraplanar gas is, however, not high and is more appropriate for the low-SFR. Fig. 7 and Fig. 8 show observations of IC 1711 as green contours.

Above the galaxy center (major-axis 0-1.5 kpc) and in the adjacent region (1.5-3 kpc) the $[NII]/H\alpha$ - $[OIII]/H\beta$ values are centered on the Allen et al. (2008) shock models (see green contours in Fig. 7). Similarly, these regions have high $\sigma_{H\alpha}$ and exclusively higher $[SII]/H\alpha$. The only other galaxy with exclusively high line ratios above the disc plane is ESO484-36, which is the strongest SFR target in the sample and hosts a very strong biconical outflow. ESO484-36 has the brightest $H\alpha$ surface brightness above the midplane. While IC 1711 has relatively weak extraplanar emission, the gas that is present above the plane has very similar ionisation and dynamical properties as the galaxies we understand to be stronger outflows. The emission line ratios are likewise similar to strong outflows. These reason for these similarities, in absence of strong $H\alpha$ flux above the midplane, remain unclear.

4.4 Galaxy Averages for Extraplanar Emission

In Fig. 9 we show the dependence of integrated extraplanar emission ($L_{H\alpha}$) and median extraplanar $[NII]/H\alpha$ on the total SFR of each galaxy. The extraplanar gas is measured only at z-axis heights that are greater than ± 2 kpc from the galaxy midplane. Also, we restrict the measurements to the central region of the extraplanar gas, which means the inner ± 1.5 kpc on the major-axis. We tested use of a wider major-axis range, but it does not significantly change Fig. 9. We find a strong correlation of galaxy SFR with total extraplanar $H\alpha$ luminosity, with Spearman correlation coefficient of 0.7 and a fitted power law of $\log(L_{H\alpha}) = 2.3 \log(\text{SFR}) + 37.6$. This result is similar to Lu et al. (2023), who found more extended $H\alpha$ emission in higher SFR galaxies.

Several authors conclude that the extraplanar $H\alpha$ emission around star forming galaxies is consistent with being driven by feedback (e.g. Levy et al. 2019; Lu et al. 2023; González-Díaz et al. 2024). Energy injected from supernovae, cosmic rays, and radiation pressure all increase with SFR (reviewed in Thompson & Heckman 2024), which would therefore generate brighter gas emission above higher SFR systems. Our observed correlation between $H\alpha$ luminosity and SFR is consistent with this. For supernova-driven winds the energy injection into the outflow scales linearly with the SFR (e.g. Thompson

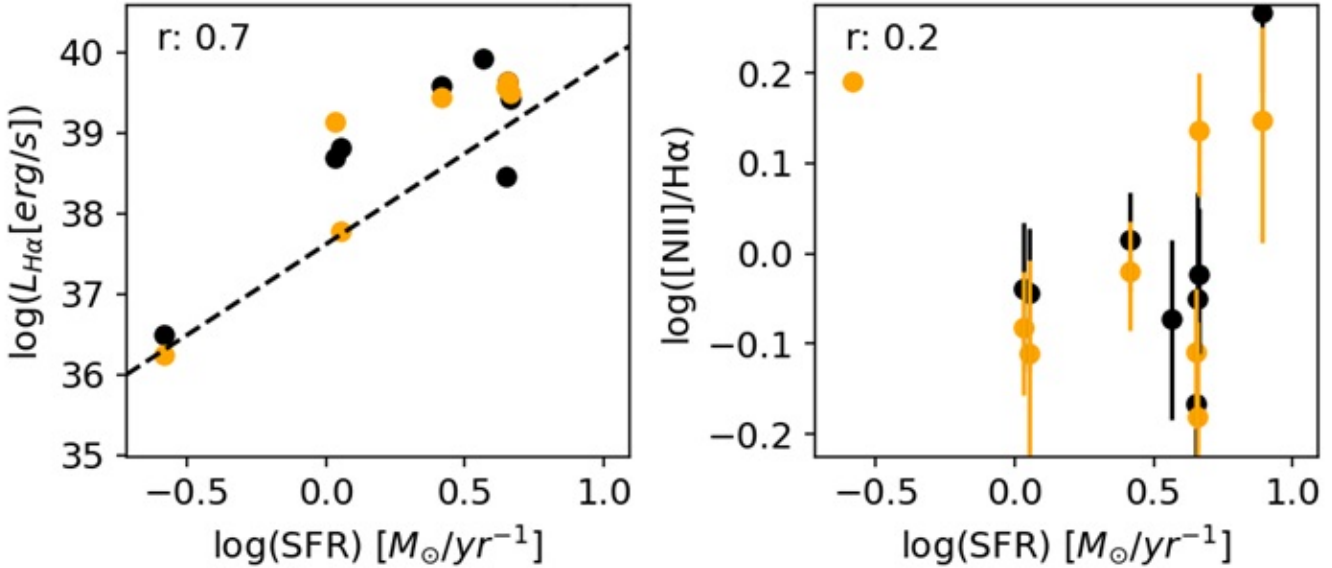


Figure 9. Measurements of SFR against extraplanar H α luminosity ($L_{H\alpha}$) and SFR against [NII]/H α for the extraplanar regions across our galaxy sample. The extraplanar gas measurements are made for gas at larger distance from the galaxy midplane than ± 2 kpc, and only in the central region of the extraplanar emission ($\pm 0.1-1.5$ kpc). This represents the brightest part of the extraplanar gas in all targets, except for NGC 3957 (discussed above). We display measurements made above (black points) and below (orange points) the midplane of each galaxy. A spearman rank correlation coefficient is indicated in the top left corner of each plot.

& Heckman 2024). If we make a somewhat simplistic assumption that outflow energy scales primarily with mass in the outflow, then we, likewise, expect a linear relationship of outflow mass with SFR (similar to results in Reichardt Chu et al. 2025). The mass of ionised gas depends on $L_{H\alpha}/n_e$, where n_e is the electron density. If n_e of the outflow increases with SFR of the galaxy, then a power-law that is near to ~ 2 for the relationship between SFR and $L_{H\alpha}$ is needed for mass in the outflow to scale linearly with SFR. This would be consistent with the power-law in Fig. 9, which implies that our power-law is consistent with extraplanar emission, in these galaxies, being driven by stellar feedback.

Recently, Mazzilli Ciraulo et al. (2025) reports the first well resolved n_e profile that extends deep into an outflow ($z \sim 6$ kpc), using GECKOS observations of NGC 4666 (included in our sample). At the least, these works show that high electron density is found in winds, which would be consistent with a linear relationship of outflow mass with SFR in GECKOS targets.

The relationship between [NII]/H α and SFR does not show a simple power-law behavior. Only two galaxies with strong evidence for outflows, ESO 079-003 and ESO 484-036, have elevated extraplanar [NII]/H α line ratios. NGC 3957, which we have previously discussed as having several differences, also has an elevated extraplanar [NII]/H α value. The majority of the sample, however, has low [NII]/H α values that are below unity. The differences in the extremes of the distribution of the emission line diagnostics found in Fig. 7 and Fig. 8, do not represent the bulk of the gas. This can be seen in the individual plots available in the Appendix, which color points based on distance to the galaxy. These show that the highest line ratios, where these differences emerge, occur in a fainter gas found at a larger distance to the galaxy.

Fig. 9 also suggests that changes in H α flux do not necessarily drive changes in [NII]/H α . While the total flux of H α above the plain appears explainable, the line ratios of extraplanar gas are not so easily described. This may simply reflect that no one phenomenon

cleanly explains all ionization mechanism in extraplanar gas around galaxies.

5 DISCUSSION & CONCLUSIONS

In this paper, we use observations from the GECKOS survey to analyse the properties of emission lines from ionised gas in galaxies. We use the first nine star forming galaxies observed. We compared extraplanar gas properties of above the midplane of starburst galaxies to those of main-sequence. We find that extraplanar emission is ubiquitous in our sample and often extends well beyond ± 2 kpc from the disk midplane. We find that the surface brightness and luminosity of extraplanar gas in galaxies correlates strongly with SFR of the galaxy, consistent with previous studies on the extraplanar emission in galaxies (e.g. Rossa & Dettmar 2003; Levy et al. 2019; Lu et al. 2023).

5.1 Velocity dispersion maps are good indicators of large biconical winds

Our sample includes 3 galaxies that have previously been identified as hosting outflows (ESO 484-036, NGC 5775 and NGC 4666). Additionally, ESO 079-003 shows extended extraplanar emission with a centralised high velocity dispersion structure and an X-shaped [NII]/H α morphology (shown in Fig. 3). These features are all characteristic of an outflow. These outflow galaxies have $SFR/M_{star} > 0.1$ Gyr $^{-1}$, which previous samples show is more probable to have outflows (Reichardt Chu et al. 2025).

McPherson et al. (2023) argue that elevated velocity dispersion in extraplanar gas is a good indicator of outflows. They also suggest that the conical shape in velocity dispersion maps from integral field spectroscopy observations can distinguish emission associated

with an outflow from ambient extraplanar gas. In our 500 pc resolution velocity dispersion maps (Fig. 4), we find velocity dispersions exceeding 150 km s^{-1} for our $\text{SFR} < 5 M_{\odot} \text{ yr}^{-1}$ outflowing galaxies. Similar dispersions are observed in other edge-on outflowing galaxies, such as Mrk148 (McPherson et al. 2023), ESO338-04 (Bik et al. 2018), and NGC 4383 (Watts et al. 2024). Moreover, when the outflow is fully covered in the MUSE mosaic we find a similar biconical shape. By contrast, high dispersions are rare in main-sequence galaxies.

Our results suggest that ionized gas velocity dispersion is an effective diagnostic for identifying candidate outflows for edge-on galaxies with IFS observations. In this case, elevated velocity dispersion with a biconical shape, when seen above a strong starburst (or AGN) in the disk, can trace outflow gas. Inside the conical outflows, the measured ionized-gas velocity dispersion is expected to be a product of both internal bulk motion of gas and the expansion of the bicone. A sufficiently high spectral resolution ($R \gtrsim 7,000$) would resolve the multipeaked emission line profiles needed to characterise this expansion (e.g. Westmoquette et al. 2008; McPherson et al. 2023).

5.2 Ionization of extraplanar gas does not vary heavily across a large range of SFR

Many studies have explored the ionisation of extraplanar gas in various galaxy samples (e.g. Collins & Rand 2001; Sharp & Bland-Hawthorn 2010; Ho et al. 2016; López-Cobá et al. 2019; Boettcher et al. 2019). These studies generally find increased ionization at larger distances from the galaxy midplane. This trend may reflect the growing contribution of shocks as an ionisation mechanism away from the midplane (e.g. Collins & Rand 2001), or it could reflect radiation field hardening at larger minor axis heights due to reduced shielding (see discussion in Kewley et al. 2019b). A mixture of both of these effects is also plausible.

Due to the larger energy and momentum associated to biconical outflows, one might expect that the ionisation properties in strong galactic winds above starburst galaxies to differ from that of the extraplanar gas above main-sequence galaxies. X-shaped $[\text{NII}]/\text{H}\alpha$ morphologies have long been an ionization signature associated with outflows (review Veilleux et al. 2005). We see this feature most clearly in ESO 079-003 for our sample (see Fig. 3). In our sample, the largest $[\text{NII}]/\text{H}\alpha$ and $[\text{SII}]/\text{H}\alpha$ values are found in the centralized extraplanar gas above ESO 484-036 and ESO 079-003. Both of these galaxies have strong velocity dispersion cones, which may suggest a stronger presence of shocks. Overall, we see the strongest shock-ionization evidence for two of our super main-sequence systems.

Conversely, NGC 4666 and NGC 5775, both outflow galaxies, only sparsely populate the shock region of the BPT parameter space. As seen in Fig. 9, only 2 of our $\text{SFR} \geq 5 M_{\odot} \text{ yr}^{-1}$ galaxies have elevated $[\text{NII}]/\text{H}\alpha$ in the outflow. We find a similar outcome for $[\text{SII}]/\text{H}\alpha$. Moreover, Bik et al. (2018) find low extraplanar $[\text{SII}]/\text{H}\alpha$ and low $[\text{NII}]/\text{H}\alpha$ in outflowing starburst galaxy ESO338-IG04. Despite these ratios, they do identify shocks with the $[\text{OI}]$ line at large distances from the galaxy. We will consider GECKOS observations of $[\text{OI}]$ in a future work.

We also find that our main sequence ($\text{SFR} < 5 M_{\odot} \text{ yr}^{-1}$) galaxies show extraplanar line ratios high enough ($[\text{NII}]/\text{H}\alpha > 1$) to be consistent with shock models by (e.g. Allen et al. 2008) (see Figs. 7 & 8). Above the galaxy center the majority of spaxels for high and low SFR are in similar regions of the $[\text{NII}]/\text{H}\alpha$ - $[\text{OIII}]/\text{H}\beta$ sequence, and main-sequence galaxies span a similar range of $[\text{SII}]/\text{H}\alpha$ and the that of starbursts. Although some minor differences in line ratio distributions are observable between the high and low SFR galaxies in

Fig. 7, our analysis has not revealed any physical significance in these differences. Our findings echo results from Ho et al. (2016), who find that emission-line ratios like $[\text{NII}]/\text{H}\alpha$ are not sufficient alone for separating galaxies with and without strong winds. The key difference appears to be in kinematics rather than ionisation, which Fig. 8 illustrates.

Levy et al. (2019) argue, based on the kinematics of edge-on galaxies, that feedback drives the majority of extraplanar emission in star forming galaxies, even in main-sequence galaxies. The correlation of extraplanar $\text{H}\alpha$ luminosity (Fig. 9), $\text{H}\alpha$ surface brightness (Fig. 6) and $\text{H}\alpha$ scale-height (Li et al. 2016) all with SFR are consistent with a picture in which feedback drives extraplanar emission in all star forming galaxies. Observations suggest that there is a shallow-slope relating Σ_{SFR} to the outflowing velocity of gas launched in winds (e.g. Reichardt Chu et al. 2025). Even modest levels of star formation ($\Sigma_{\text{SFR}} \sim 0.1 M_{\odot} \text{ yr}^{-1} \text{ kpc}^{-2}$) are observed to have ionized gas velocities of $\sim 100\text{--}200 \text{ km s}^{-1}$ (e.g. Reichardt Chu et al. 2025), which would potentially drive gas upward and could create a shock against the inner CGM.

Aside from the explanation, from a purely observational view, our results suggest that ionised gas line ratios alone are insufficient to identify the presence of outflows. Using elevated $[\text{NII}]/\text{H}\alpha$ or $[\text{SII}]/\text{H}\alpha$ to indicate outflows would likely underestimate the number of systems that show outflows. A combined analysis of velocity dispersion and line-ratios would improve results, but resolved imaging that indicates a conical shape in $[\text{NII}]/\text{H}\alpha$ and/or $\sigma_{\text{H}\alpha}$ provides a more complete selection.

5.3 IC 1711: A possible relic outflow

IC 1711 shows high velocity dispersion above the galaxy center and enhanced emission line ratios in the central part of the extraplanar gas, but lacks bright extraplanar emission. IC 1711 has the second lowest SFR in our sample, with $\text{SFR} \sim 1.1 M_{\odot} \text{ yr}^{-1}$, and low specific star formation rate, $\text{SFR}/M_{\text{star}} \sim 0.02 \text{ Gyr}^{-1}$. It would be very different than previous observations for this this low star formation to drive an outflow (e.g. Förster Schreiber et al. 2019; Reichardt Chu et al. 2025). Moreover, there is no evidence of a presently luminous AGN, see BPT in Appendix. Unless there is a high central Σ_{SFR} in this galaxy that our Σ_{SFR} measurements are insensitive to, The morphology of the velocity dispersion and line-ratio of IC 1711 contrasts with the patterns seen for the high SFR galaxies, such as ESO 484-036.

If our SFR measurement is not a significant underestimate, one possible explanation for the behavior of IC 1711 could be that some extraplanar emission may trace relic gas from stronger outflows in the past. Pillepich et al. (2021) show, in TNG simulations, that over pressurized, high ionization cones in Milky Way mass systems persist after the feeding of the galactic wind turns off. In these simulations the outflow is driven by an AGN, and after it turns off a high ionization cone remains for 10–100 Myr. Pillepich et al. (2021) argue that these are similar to the large X-ray and γ -ray bubbles that extend out from the center of the Milky Way, called “Fermi Bubbles” (Su et al. 2010). Such bubbles could generate changes to both internal gas kinematics and emission line ratios. González-Díaz et al. (2024) studies emission line ratios of 9 edge-on galaxies with similar SFR to IC 1711. They likewise show at least one target has a similar line-ratio morphology. Deep IFS observations of edge-on low-SFR systems may, therefore, reveal evidence of past outflow activity. This opens an opportunity to study the time evolution of outflows. More work studying these systems would be helpful to understand their nature.

Above, we discuss that the combined use of gas velocity dispersion and $[\text{NII}]/\text{H}\alpha$ line ratios is a useful tool to identify outflows. Such

a selection would include a galaxy like IC 1711. The additional information from the H α flux, would likely conclude that the mass-outflow rate derived for this target would be very low. It would, therefore, not necessarily be problematic to select targets like IC 1711 with stronger outflow systems, as long as authors considered the a mass tracer, like H α flux.

The total GECKOS sample includes 36 galaxies, \sim 24 of which are star forming systems. This work represents an initial analysis. Whilst clear kinetic signatures of galactic winds appear in this sample, caveats remain. Future work with the complete GECKOS survey will improve statistics enable analysis of mass-loading, energy-loading, and the detailed physics of galactic winds.

ACKNOWLEDGEMENTS

Based on observations made with ESO Telescopes at the La Silla Paranal Observatory under program ID 110.24AS. We wish to thank the ESO staff, and in particular the staff at Paranal Observatory, for carrying out the GECKOS observations. This paper makes use of services that have been provided by AAO Data Central (datacentral.org.au). This research has made use of the NASA/IPAC Extragalactic Database (NED; <https://ned.ipac.caltech.edu/>) operated by the Jet Propulsion Laboratory, California Institute of Technology, under contract with the National Aeronautics and Space Administration. This research has made use of the NASA/IPAC Infrared Science Archive, which is funded by the National Aeronautics and Space Administration and operated by the California Institute of Technology. Part of this research was conducted by the Australian Research Council Centre of Excellence for All Sky Astrophysics in 3 Dimensions (ASTRO 3D), through project number CE170100013. MM acknowledges support from the UK Science and Technology Facilities Council through grant ST/Y002490/1. FP acknowledges support from the Horizon Europe research and innovation programme under the Maria Skłodowska-Curie grant “TraNSlate” No 101108180.

DATA AVAILABILITY

The data is available in the ESO archive. The emission line fits may be available by contacting Deanne Fisher (dfisher@swin.edu.au).

REFERENCES

Allen M. G., Groves B. A., Dopita M. A., Sutherland R. S., Kewley L. J., 2008, *ApJS*, **178**, 20

Bacon R., Piqueras L., Conseil S., Richard J., Shepherd M., 2016, MPDAF: MUSE Python Data Analysis Framework, Astrophysics Source Code Library, record ascl:1611.003 (ascl:1611.003)

Baldwin J. A., Phillips M. M., Terlevich R., 1981, *PASP*, **93**, 5

Bik A., Östlin G., Menacho V., Adamo A., Hayes M., Herenz E. C., Melinder J., 2018, *A&A*, **619**, A131

Bittner A., et al., 2019, *A&A*, **628**, A117

Bland-Hawthorn J., Gerhard O., 2016, *ARA&A*, **54**, 529

Blum R. D., et al., 2016, in American Astronomical Society Meeting Abstracts #228. p. 317.01

Boettcher E., Gallagher III J. S., Zweibel E. G., 2019, *ApJ*, **885**, 160

Bruzual G., Charlot S., 2003, *MNRAS*, **344**, 1000

Cappellari M., 2017, *MNRAS*, **466**, 798

Cappellari M., 2023, *MNRAS*, **526**, 3273

Cappellari M., Copin Y., 2003, *MNRAS*, **342**, 345

Cappellari M., Emsellem E., 2004, *PASP*, **116**, 138

Cardelli J. A., Clayton G. C., Mathis J. S., 1989, *ApJ*, **345**, 245

Chambers K. C., et al., 2016, *arXiv e-prints*, p. arXiv:1612.05560

Chisholm J., Tremonti C. A., Leitherer C., Chen Y., Wofford A., Lundgren B., 2015, *ApJ*, **811**, 149

Chisholm J., Tremonti C. A., Leitherer C., Chen Y., 2017, *MNRAS*, **469**, 4831

Cluver M. E., Jarrett T. H., Dale D. A., Smith J. D. T., August T., Brown M. J. I., 2017, *ApJ*, **850**, 68

Collins J. A., Rand R. J., 2001, *ApJ*, **551**, 57

Dahlem M., Petr M. G., Lehnert M. D., Heckman T. M., Ehle M., 1997, *A&A*, **320**, 731

Davies R. L., Rich J. A., Kewley L. J., Dopita M. A., 2014, *MNRAS*, **439**, 3835

Dettmar R. J., 1990, *A&A*, **232**, L15

Dey A., et al., 2019, *AJ*, **157**, 168

Dopita M. A., Sutherland R. S., 1996, *ApJS*, **102**, 161

ESO CPL Development Team 2015, Astrophysics Source Code Library, p. ascl:1504.003

Emsellem E., et al., 2022, *A&A*, **659**, A191

Fisher D. B., et al., 2025, *MNRAS*, **538**, 3068

Flores-Fajardo N., Morisset C., Stasińska G., Binette L., 2011, *MNRAS*, **415**, 2182

Förster Schreiber N. M., et al., 2019, *ApJ*, **875**, 21

Fraser-McKelvie A., et al., 2025, *A&A*, **700**, A237

González-Díaz R., Rosales-Ortega F. F., Galbany L., 2024, *A&A*, **691**, A25

Haffner L. M., et al., 2009, *Reviews of Modern Physics*, **81**, 969

Hamel-Bravo M. J., et al., 2024, *MNRAS*, **530**, 3855

Heald G. H., Rand R. J., Benjamin R. A., Collins J. A., Bland-Hawthorn J., 2006, *ApJ*, **636**, 181

Heald G. H., et al., 2022, *MNRAS*, **509**, 658

Heckman T. M., Alexandroff R. M., Borthakur S., Overzier R., Leitherer C., 2015, *ApJ*, **809**, 147

Ho I. T., et al., 2014, *MNRAS*, **444**, 3894

Ho I. T., et al., 2016, *MNRAS*, **457**, 1257

Kauffmann G., et al., 2003, *MNRAS*, **346**, 1055

Kewley L. J., Dopita M. A., Sutherland R. S., Heisler C. A., Trevena J., 2001, *ApJ*, **556**, 121

Kewley L. J., Dopita M. A., Leitherer C., Davé R., Yuan T., Allen M., Groves B., Sutherland R., 2013, *The Astrophysical Journal*, **774**, 100

Kewley L. J., Nicholls D. C., Sutherland R. S., 2019a, *ARA&A*, **57**, 511

Kewley L. J., Nicholls D. C., Sutherland R. S., 2019b, *ARA&A*, **57**, 511

Kuntschner H., et al., 2006, *MNRAS*, **369**, 497

Levy R. C., et al., 2019, *ApJ*, **882**, 84

Li J.-T., et al., 2016, *MNRAS*, **456**, 1723

López-Cobá C., Sánchez S. F., Bland-Hawthorn J., Moiseev A. V., Cruz-González I., García-Benito R., Barrera-Ballesteros J. K., Galbany L., 2019, *MNRAS*, **482**, 4032

López-Cobá C., et al., 2020, *AJ*, **159**, 167

Lopez S., Lopez L. A., Thompson T. A., Leroy A. K., Bolatto A. D., 2025, *ApJ*, **989**, 100

Lu L.-Y., et al., 2023, *MNRAS*, **519**, 6098

Lupton R., Blanton M. R., Fekete G., Hogg D. W., O’Mullane W., Szalay A., Wherry N., 2004, *PASP*, **116**, 133

Mazzilli Ciraulo B., et al., 2025, *MNRAS*,

McPherson D. K., et al., 2023, *MNRAS*, **525**, 6170

Melchior A.-L., Combes F., 2007, *MNRAS*, **381**, 1508

Naab T., Ostriker J. P., 2017, *ARA&A*, **55**, 59

Pillepich A., Nelson D., Truong N., Weinberger R., Martin-Navarro I., Springel V., Faber S. M., Hernquist L., 2021, *Monthly Notices of the Royal Astronomical Society*, **508**, 4667

Rand R. J., 1996, *ApJ*, **462**, 712

Reichardt Chu B., et al., 2022, *MNRAS*, **511**, 5782

Reichardt Chu B., et al., 2024, *arXiv e-prints*, p. arXiv:2402.17830

Reichardt Chu B., et al., 2025, *MNRAS*, **536**, 1799

Rich J. A., Dopita M. A., Kewley L. J., Rupke D. S. N., 2010, *ApJ*, **721**, 505

Rich J. A., Kewley L. J., Dopita M. A., 2011, *ApJ*, **734**, 87

Rich J. A., Kewley L. J., Dopita M. A., 2015, *ApJS*, **221**, 28

Rossa J., Dettmar R. J., 2003, *A&A*, **406**, 493

Rutherford T. H., et al., 2025, [A&A](#), **703**, A206

Sánchez S. F., 2020, [ARA&A](#), **58**, 99

Shapiro P. R., Field G. B., 1976, [ApJ](#), **205**, 762

Sharp R. G., Bland-Hawthorn J., 2010, [ApJ](#), **711**, 818

Shopbell P. L., Bland-Hawthorn J., 1998a, [The Astrophysical Journal](#), **493**, 129

Shopbell P. L., Bland-Hawthorn J., 1998b, [ApJ](#), **493**, 129

Somerville R. S., Davé R., 2015, [Annual Review of Astronomy and Astrophysics](#), **53**, 51

Stein Y., et al., 2019, [A&A](#), **623**, A33

Su M., Slatyer T. R., Finkbeiner D. P., 2010, [ApJ](#), **724**, 1044

Theureau G., 2023, Cahiers Clairaut: Bulletin du Comité de Liaison Enseignants et Astronomes, **183**, 10

Thompson T. A., Heckman T. M., 2024, [ARA&A](#), **62**, 529

Tully R. B., et al., 2023, [ApJ](#), **944**, 94

Vazdekis A., Arimoto N., 1999, [ApJ](#), **525**, 144

Vazdekis A., Sánchez-Blázquez P., Falcón-Barroso J., Cenarro A. J., Beasley M. A., Cardiel N., Gorgas J., Peletier R. F., 2010, [MNRAS](#), **404**, 1639

Veilleux S., Rupke D. S., 2002, [ApJ](#), **565**, L63

Veilleux S., Cecil G., Bland-Hawthorn J., 2005, [Annual Review of Astronomy and Astrophysics](#), **43**, 769–826

Veilleux S., Maiolino R., Bolatto A. D., Aalto S., 2020a, [A&ARv](#), **28**, 2

Veilleux S., Maiolino R., Bolatto A. D., Aalto S., 2020b, [A&ARv](#), **28**, 2

Walcher C. J., Coelho P., Gallazzi A., Charlot S., 2009, [MNRAS](#), **398**, L44

Watts A. B., et al., 2024, [MNRAS](#), **530**, 1968

Weilbacher P. M., et al., 2020, [A&A](#), **641**, A28

Westmoquette M. S., Smith L. J., Gallagher J. S., 2008, [MNRAS](#), **383**, 864

Westmoquette M. S., Smith L. J., Gallagher J. S. I., 2011, [MNRAS](#), **414**, 3719

van de Sande J., Fraser-McKelvie A., Fisher D. B., Martig M., Hayden M. R., the GECKOS Survey collaboration 2023, [arXiv e-prints](#), p. [arXiv:2306.00059](#)

APPENDIX A: APPENDIX A

A1 BPT line diagnostics for individual galaxies

The following section lists our [OIII]/H β BPT diagrams made for each of our individual galaxies. Compared to Fig. 7 and Fig. 8, these plots display scatter points for individual pixels. The color of each point represents the corresponding pixel’s projected minor axis separation from its galaxy’s midplane. We note that there is generally a positive correlation between line ratios, dispersion, and minor axis height in these diagrams.

This paper has been typeset from a $\text{\TeX}/\text{\LaTeX}$ file prepared by the author.

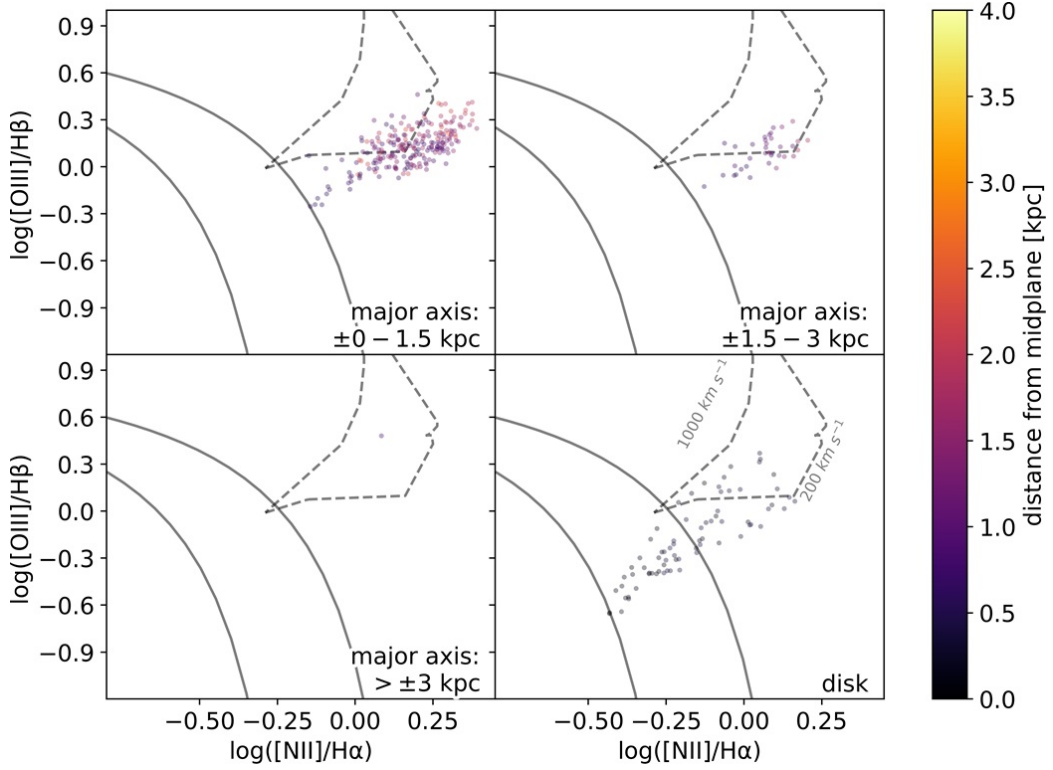


Figure A1. A set of $[\text{NII}]/\text{H}\alpha$ against $[\text{OIII}]/\text{H}\beta$ BPT diagrams for ESO 484-036. Similar to what is shown in Fig. 7, BPT diagrams are given for pixels in the galaxy's major axis position: $\pm 0-1.5$ kpc, major axis position: $\pm 1.5-3$ kpc, major axis position: $>|3|$ kpc, and disk regions. Individual pixels are represented by separate scatter points, where the color of each point represents the pixel's minor axis height. Note that the displayed trend lines and grid are the same as the ones shown in Fig. 7. This figure is discussed in Section 4.1.

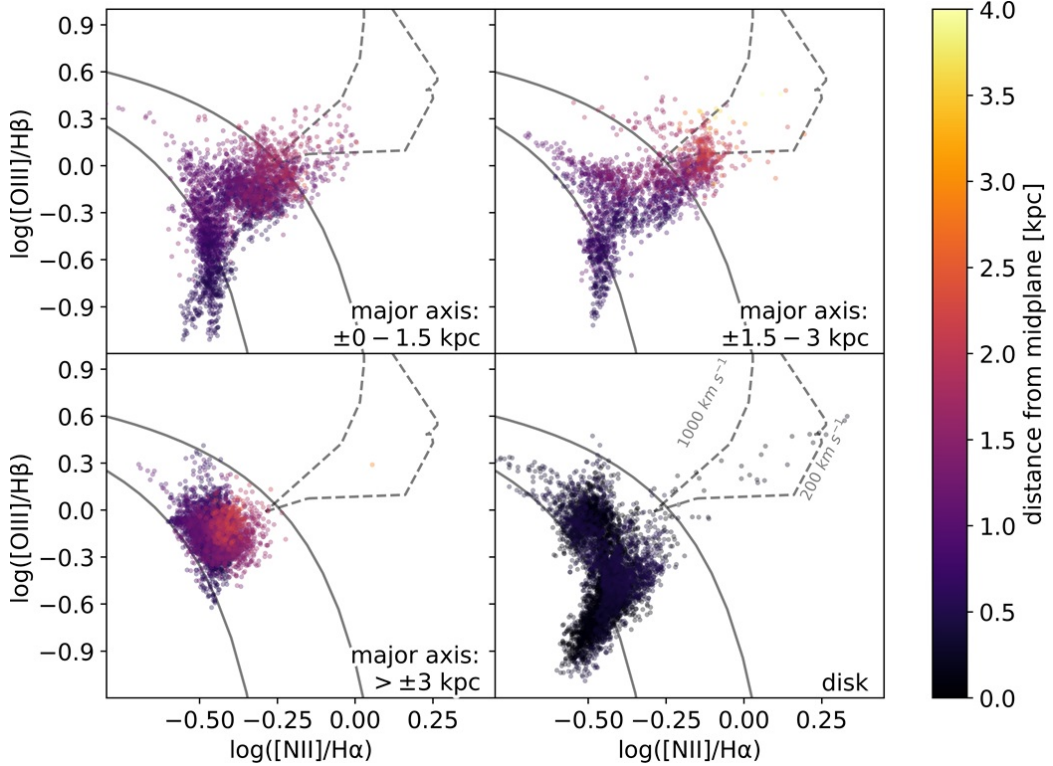


Figure A2. A set of $[\text{NII}]/\text{H}\alpha$ against $[\text{OIII}]/\text{H}\beta$ BPT diagrams made for NGC 4666. The format is the same as the one used in Fig. A1. This figure is discussed in Section 4.1.

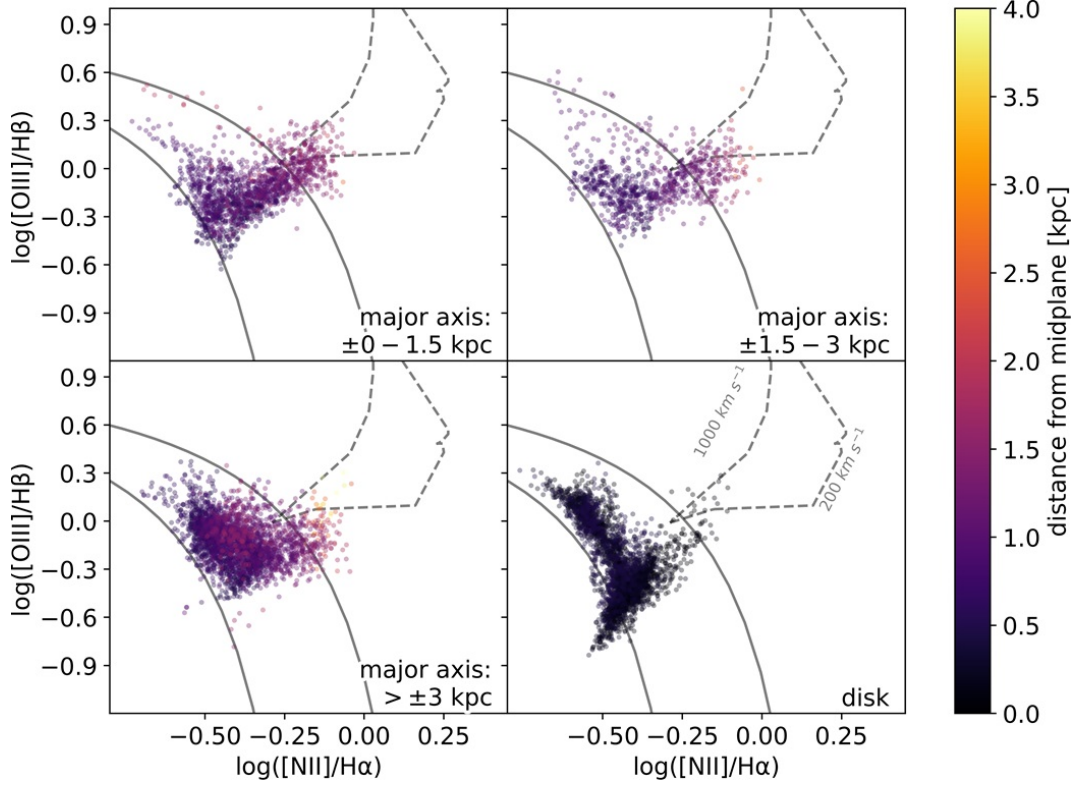


Figure A3. A set of $[\text{NII}]/\text{H}\alpha$ against $[\text{OIII}]/\text{H}\beta$ BPT diagrams made for NGC 5775. The Format is the same as the one used in Fig. A1. This figure is discussed in Section 4.1.

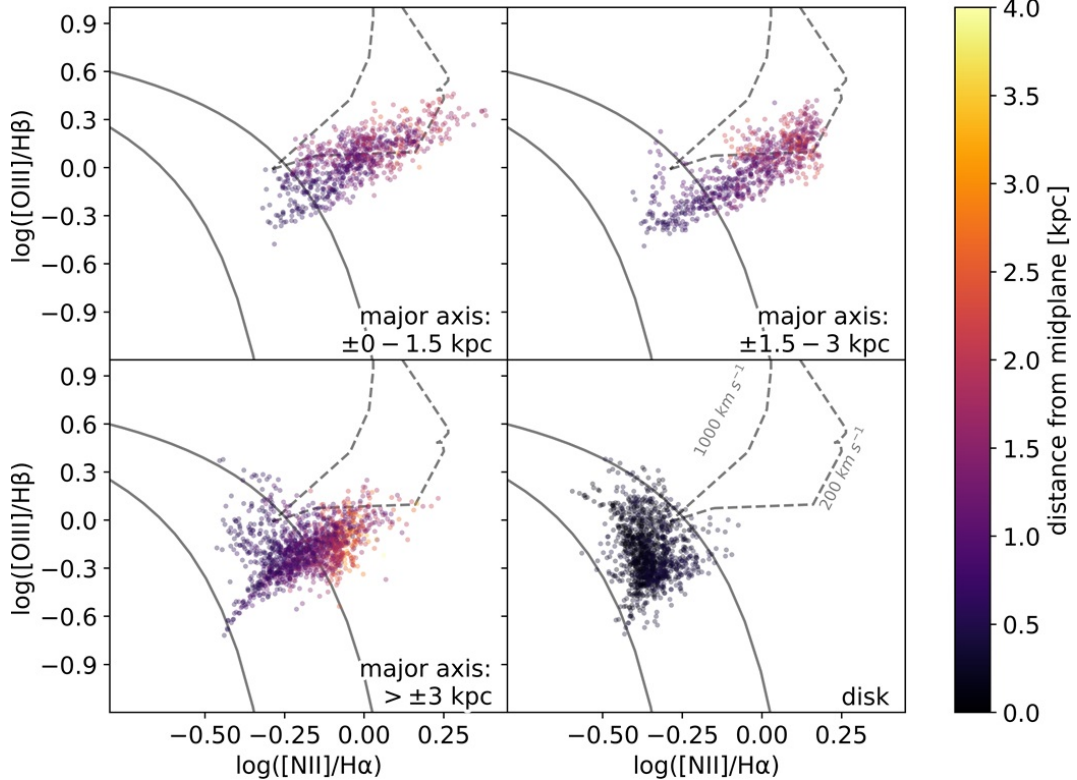


Figure A4. A set of $[\text{NII}]/\text{H}\alpha$ against $[\text{OIII}]/\text{H}\beta$ BPT diagrams made for ESO 079-003. The format is the same as the one used in Fig. A1. This figure is discussed in Section 4.1.

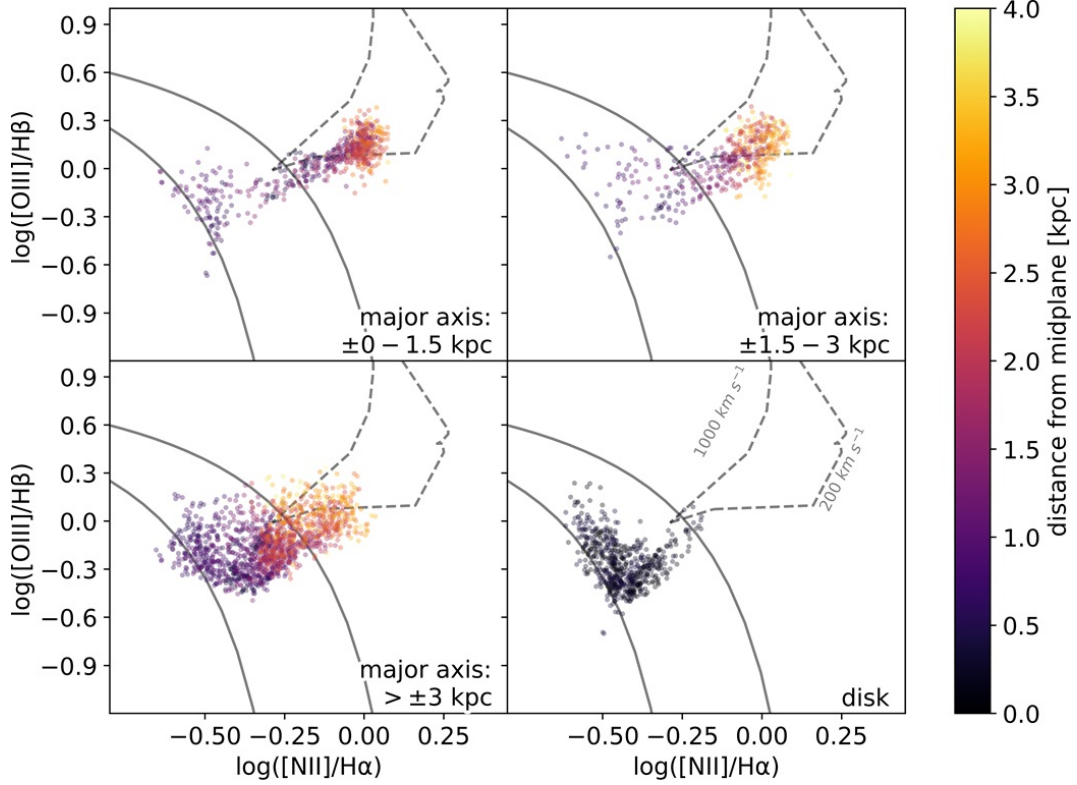


Figure A5. A set of $[\text{NII}]/\text{H}\alpha$ against $[\text{OIII}]/\text{H}\beta$ BPT diagrams made for ESO 120-016. The format is the same as the one used in Fig. A1. This figure is discussed in Section 4.2.

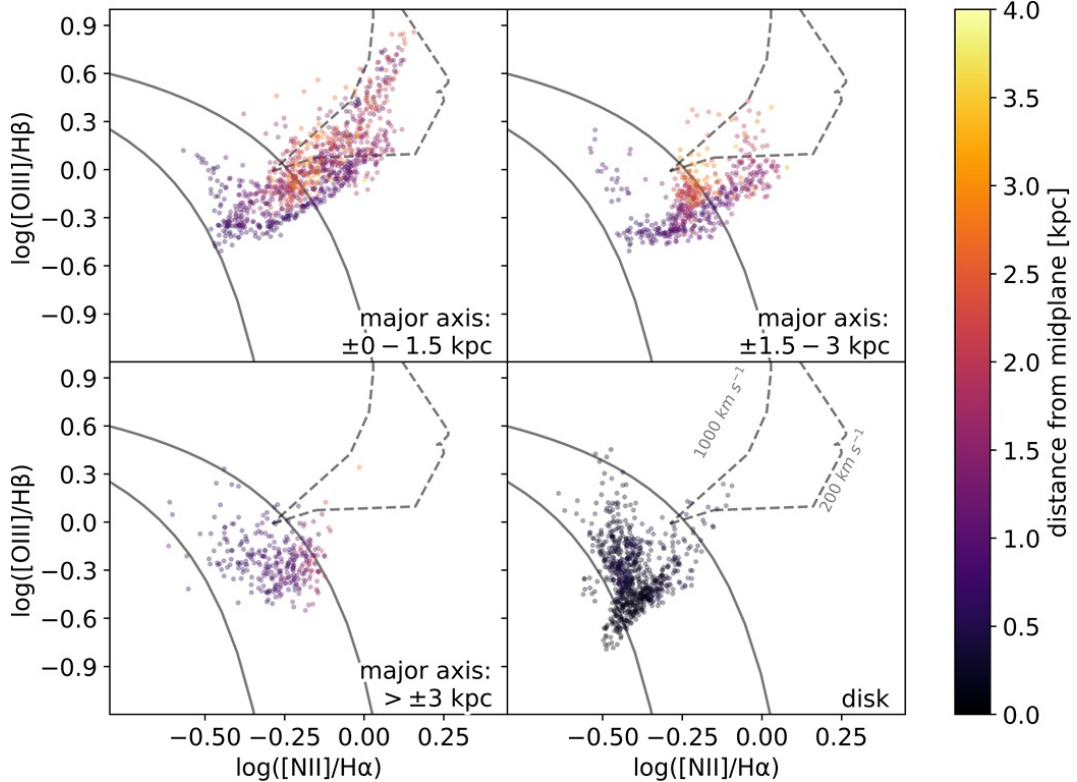


Figure A6. A set of $[\text{NII}]/\text{H}\alpha$ against $[\text{OIII}]/\text{H}\beta$ BPT diagrams made for UGC 00903. The format is the same as the one used in Fig. A1. This figure is discussed in Section 4.2.

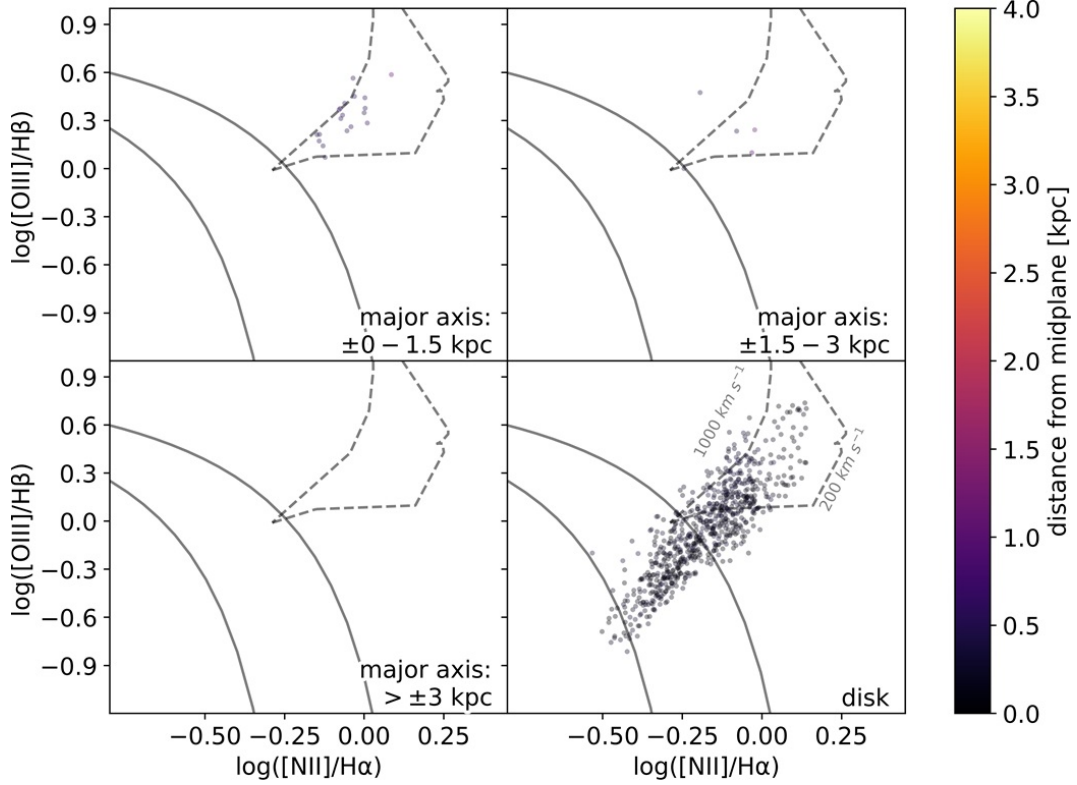


Figure A7. A set of $[\text{NII}]/\text{H}\alpha$ against $[\text{OIII}]/\text{H}\beta$ BPT diagrams made for NGC 3957. The format is the same as the one used in Fig. A1. This figure is discussed in Section 4.2.

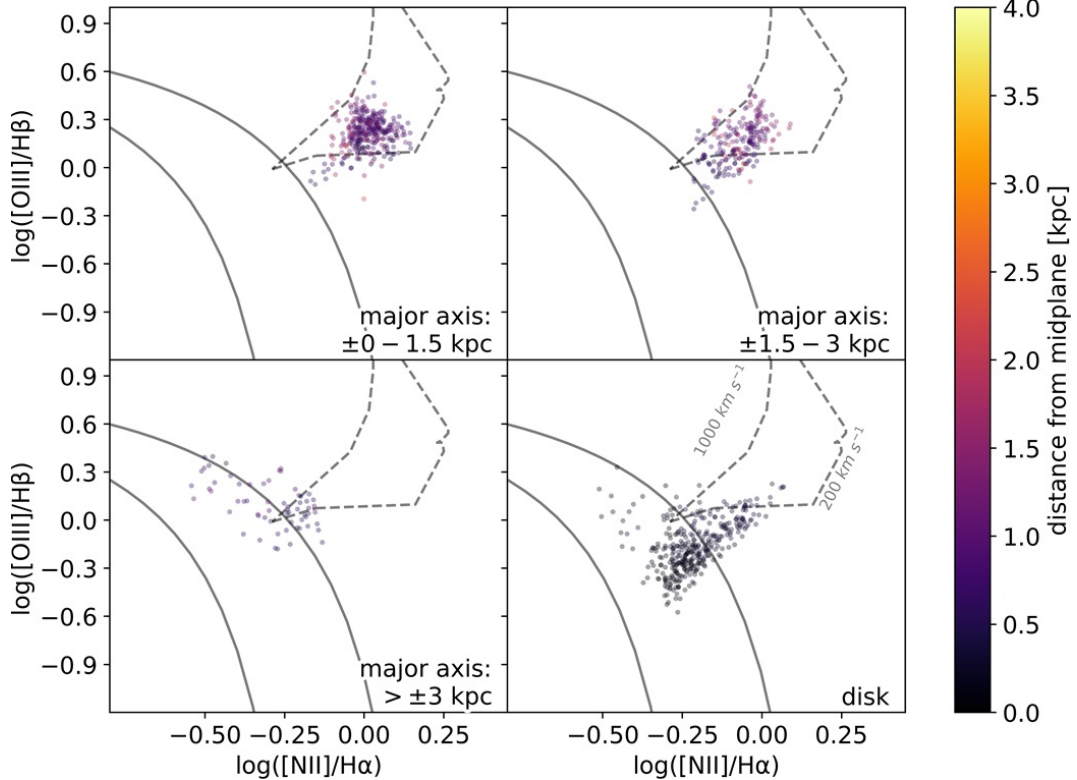


Figure A8. A set of $[\text{NII}]/\text{H}\alpha$ against $[\text{OIII}]/\text{H}\beta$ BPT diagrams made for IC 1711. The Format is the same as the one used in Fig. A1. This figure is discussed in Section 4.1.

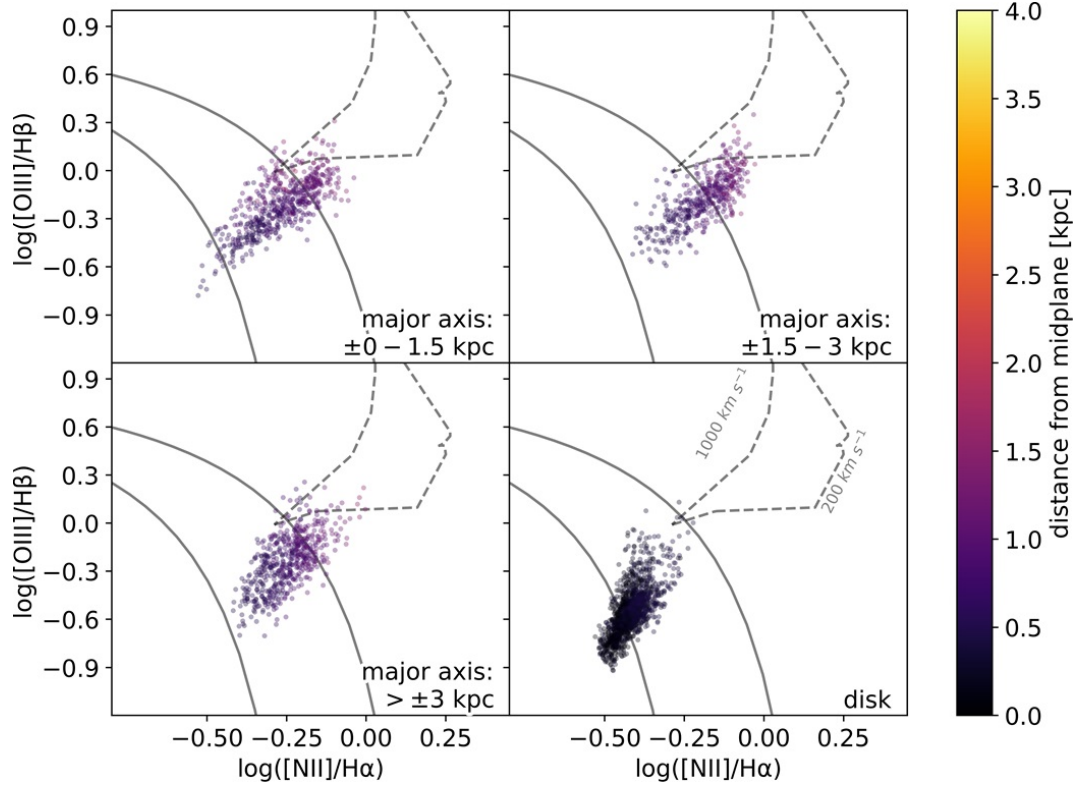


Figure A9. A set of $[\text{NII}]/\text{H}\alpha$ against $[\text{OIII}]/\text{H}\beta$ BPT diagrams made for NGC 3279. The format is the same as the one used in Fig. A1. This figure is discussed in Section 4.2.